



universität  
wien

# DIPLOMARBEIT

Titel der Diplomarbeit

On the influence of hydrogen on the stability of lattice  
defects in metals

angestrebter akademischer Grad

Magister der Naturwissenschaften (Mag. rer. nat.)

Verfasser:	Matthias Bönisch
Matrikelnummer:	0503080
Studienrichtung (lt. Studienblatt):	Physik
Betreuer:	Ao. Univ.-Prof. Dr. Gerhard Krexner
Mitbetreuer:	Ao. Univ.-Prof. Dr. Michael Zehetbauer

Wien, März 2011

# Abstract

This work investigates the influence of hydrogen (H) on the formation and thermal stability of lattice defects in palladium (Pd). High Pressure Torsion (HPT) was chosen as technique for introduction of lattice defects. HPT belongs to the family of Severe Plastic Deformation techniques which allow to reduce grain sizes down to the nanometer range. They all are based on the same principle, i. e. high grade plastic deformation at low homologous temperature at hydrostatic pressure without modification of sample geometry. Pd was chosen because the Pd-H system is the best-studied of all metal-hydrogen systems and comprehensive literature is available.

Samples of Pd (99.95 at%) were loaded with H up to a concentration of  $x = [\text{H}]/[\text{Pd}] = 0.78$  using a Sieverts-type apparatus available at the Faculty of Physics of the University of Vienna. Samples were subsequently deformed by HPT at different temperatures and characterized by various methods: Differential scanning calorimetry was used to follow the evolution of the system with temperature; investigation with the scanning electron microscope and high-precision density measurements were used to determine vacancy concentrations. For a further characterization of non HPT-deformed palladium hydride desorption as well as microhardness measurements were performed.

Additionally, first H-loading tests on titanium were carried out successfully with the Sieverts apparatus and the titanium hydride prepared in this way was deformed by HPT.

In summary, it can be said that the working hypothesis, that is the stabilizing influence of H on lattice defects in metals, could be confirmed to hold within a certain temperature range. As could be shown the deformation temperature is a crucial parameter for this effect.

# Kurzfassung

Diese Arbeit untersucht den Einfluss von Wasserstoff (H) auf die Bildung und thermische Stabilität von Gitterdefekten in Palladium (Pd). Als Methode zur Erzeugung von Gitterdefekten wurde High Pressure Torsion (HPT) gewählt. HPT wird der Gruppe der Severe Plastic Deformation-Techniken zugeordnet, welche eine Reduzierung der Korngrößen in den Nanometerbereich hinein ermöglichen. Sie alle basieren auf demselben Prinzip, nämlich der hochgradig plastischen Verformung bei niedriger homologer Temperatur unter hydrostatischem Druck ohne Veränderung der Probengeometrie. Pd wurde gewählt, weil das Pd-H-System das am besten untersuchte Metall-H-System und daher umfangreiche Literatur vorhanden ist.

Proben aus Pd (99.95 at%) wurden mit dem Sieverts-Apparat der Fakultät für Physik an der Universität Wien mit H auf eine Konzentration von  $x = [\text{H}]/[\text{Pd}] = 0.78$  beladen, anschließend bei unterschiedlichen Temperaturen HPT-verformt und mittels verschiedener Methoden charakterisiert: Dynamische Differenzkalorimetrie wurde verwendet um der Entwicklung des Systems mit der Temperatur zu folgen; Untersuchungen mit dem Rasterelektronenmikroskop und hochpräzise Dichtemessungen wurden zur Bestimmung von Leerstellenkonzentrationen verwendet. Zur weiteren Charakterisierung von nicht HPT-verformten Palladiumhydrid wurden Desorptionswägungen sowie Mikrohärtemessungen durchgeführt.

Zusätzlich wurden erste H-Beladetests an Titan erfolgreich in dem Sieverts-Apparat ausgeführt, sowie das damit erhaltene Titanhydrid mittels HPT verformt.

Zusammenfassend kann gesagt werden, dass die Arbeitshypothese, das heißt der stabilisierende Einfluss von H auf Gitterdefekte in Metallen, unter Einschränkung des Temperaturbereichs bestätigt werden konnte. Wie gezeigt werden konnte ist die Verformungstemperatur ein entscheidender Parameter für diesen Effekt.

# Contents

<b>Abstract</b>	<b>i</b>
<b>List of abbreviations</b>	<b>iv</b>
<b>1 Introduction and aim of work</b>	<b>1</b>
<b>2 Experimental methods and theoretical background</b>	<b>4</b>
2.1 Lattice defects in metals . . . . .	4
2.1.1 Vacancy formation and its consequences on density and lattice parameter	9
2.2 Diffusion . . . . .	10
2.3 Deformation of a solid body . . . . .	11
2.3.1 The initial linear range – elastic deformation . . . . .	12
2.3.2 Plastic deformation . . . . .	13
2.4 Severe plastic deformation . . . . .	16
2.4.1 Paradoxon of SPD materials . . . . .	17
2.4.2 High pressure torsion (HPT) . . . . .	19
2.5 Hydrogen in metals . . . . .	20
2.5.1 The Pd-H system . . . . .	26
2.5.2 The Ti-H system . . . . .	27
2.5.3 Diffusion of interstitial hydrogen in metals . . . . .	28
2.5.4 Fukai's concept of superabundant vacancies (SAVs) . . . . .	30
2.5.5 Formation of SAVs in PdH generated by HPT . . . . .	34
2.6 Hydrogenation using the Sieverts apparatus . . . . .	36
2.7 The microhardness test . . . . .	39
2.8 Scanning electron microscopy . . . . .	40

2.9	Thermal analysis . . . . .	41
2.9.1	Differential scanning calorimetry (DSC) . . . . .	41
2.9.2	Thermogravimetical analysis (TGA) . . . . .	42
2.10	Archimedean measurements . . . . .	43
<b>3</b>	<b>Results and discussion</b>	<b>44</b>
3.1	Material and initial sample preparation . . . . .	44
3.2	Hydrogenation of Pd and Ti . . . . .	44
3.2.1	Hydrogenation of Pd . . . . .	44
3.2.2	Hydrogenation of Ti . . . . .	47
3.3	Desorption measurements . . . . .	50
3.4	Microhardness tests . . . . .	53
3.5	Deformation by HPT . . . . .	56
3.5.1	Deformation under LN <sub>2</sub> . . . . .	56
3.5.2	Deformation under CO <sub>2</sub> . . . . .	59
3.5.3	Deformation of TiH <sub>1.91</sub> . . . . .	59
3.6	Differential scanning calorimetry (DSC) . . . . .	60
3.6.1	DSC of Pd . . . . .	60
3.6.2	DSC of Ti . . . . .	63
3.7	SEM-investigations . . . . .	66
3.8	Density measurements . . . . .	69
<b>4</b>	<b>Summary and outlook</b>	<b>73</b>
4.1	Summary . . . . .	73
4.2	Outlook . . . . .	74
<b>5</b>	<b>Appendices</b>	<b>76</b>
5.1	Appendix I . . . . .	76

5.2 Appendix II . . . . .	77
<b>References</b>	<b>79</b>
<b>Acknowledgements</b>	<b>83</b>
<b>CV</b>	<b>84</b>

## List of abbreviations

$T_m$	melting temperature in K
SPD	Severe Plastic Deformation
HPT	High Pressure Torsion
O-site	octahedral interstitial site
T-site	tetrahedral interstitial site
Vac	vacancy
SEM	Scanning Electron Microscopy
DSC	Differential Scanning Calorimetry
fcc	face centered cubic
fct	face centered tetragonal
bcc	body centered cubic
hcp	hexagonal close packed
RT	room temperature
MHT	MicroHardness Test
SAVs	SuperAbundant Vacancies
TGA	ThermoGravimetrical Analysis
TC	Temperature-Composition
PCT	Pressure-Composition-Temperature

# 1 Introduction and aim of work

In the last two decades great efforts aimed at processing of materials with crystallite sizes less than 100 nm. Methods known to enable the fabrication of bulk nanocrystalline materials immediately from the coarse-grained source materials belong to the family of Severe Plastic Deformation (SPD) [1]. The great interest in nanocrystalline materials is based on their novel properties, e. g. a unique combination of both high strength and ductility, enhanced diffusion and a shift of Debye and Curie temperatures [2,3]. SPD materials are considered to have great potential for various applications in different areas of mechanical, electrical, magnetic and biomedical engineering. However, use of nanocrystalline materials is presently restricted to low-temperature applications due to annealing processes and concomitant loss of characteristic properties. It is therefore desirable to find a way to thermally stabilize nanocrystalline structures.

It is possible to influence migration energy and hence migration temperature, as well as kinetics of lattice defects by introducing alloying atoms into the material. A shift of migration temperature and suppression of low-temperature annealing stages in alloyed aluminium and copper was already reported more than 50 years ago [4, 5]. Recently the suppression of grain growth in nanocrystalline Fe alloyed with zirconium has been reported [6]. In Fe alloyed with 1 at% Zr grain growth ceased at grain sizes four times smaller than in pure Fe during heat treatment at a homologous temperature as high as  $0.9 T_m$  ( $T_m$ ... absolute melting temperature). The effect was attributed to a reduction of grain boundary energy by segregation of Zr. Furthermore, a shift of defect annealing to higher temperatures has been documented in Ni of low grade purity compared to Ni of high grade purity [7].

Over the last years a large number of vacancies has been observed in various metal-hydrogen (M-H) systems after subjection to high  $H_2$ -pressure and high temperatures [8, 9] or various specimen preparation techniques, like electrodepositing [10] or plasma-based ion implantation [11]. In some cases the concentration of these vacancies was extraordinarily high, i. e. of the order of 10 at%. These vacancies are commonly termed SuperAbundant Vacancies (SAVs)

[12, 13] and are considered to arise from a lowering of the vacancy formation energy by segregation of H.

A theoretical model explaining the reduction of defect formation energies by segregation of solute atoms by extending the concept of Gibbs' adsorption isotherm was proposed by R. Kirchheim [14].

Alloy atoms can act as traps for defects [15] or vice versa, thereby altering defect migration enthalpies. One option is to use hydrogen (H) as the alloy element [14, 16–18]. It can be absorbed onto interstitial sites by a large number of metals [19–21] including Pd [16, 22] and is known to strongly interact with various types of lattice defects [16, 17, 19, 21–24].

For this work High Pressure Torsion (HPT) was chosen as the method to introduce lattice defects. This technique provides various benefits over other SPD methods like Accumulative Roll Bonding (ARB) [25] and Equal Channel Angular Pressing (ECAP) [26]: it permits (i) precise control of processing parameters and (ii) the possibility of processing even brittle materials like metal hydrides.

This work aims to expand the knowledge retrieved from preceding studies on the formation and annealing characteristics of lattice defects in HPT-deformed palladium hydride (PdH) [7, 16]. The main focus lies on the characterization of vacancies and vacancy-hydrogen (Vac-H) agglomerates formed during the deformation process. Three techniques were applied for this purpose: Differential Scanning Calorimetry (DSC), density measurements, and Scanning Electron Microscopy (SEM), the first being of highest importance to identify defects and investigate the behaviour of the microstructure exposed to thermal treatment. During DSC heat flow out of or into the specimen is recorded. It allows to measure (i) absolute defect densities from the total heat released during a specific annealing process and (ii) identification of defects via measurement of migration energies.

To further characterize the system desorption measurements and microhardness tests for PdH<sub>0.78</sub> are presented.

Palladium (Pd) was chosen because of its affinity for H [20] and its fast sorption kinetics. The phase diagram of the Pd-H system is rather simple: A single face centered cubic (fcc) host-metal lattice modification occurs above a temperature of  $\sim 90$  K up to a H to Pd atomic ratio of  $x = [\text{H}]/[\text{Pd}] = 1$ . The Pd-H system is the most extensively studied M-H system and comprehensive data are available.

In view of extending the investigations to other crystal structures than fcc first hydrogenation and HPT experiments were performed on pure titanium (Ti) and titanium hydride (TiH), respectively. Lattice modifications present in Ti-H (see Fig. 17) are hexagonal close packed (hcp) or body centered cubic (bcc) (both solid solutions), and fcc or face centered tetragonal (fct) (hydride phases) [27].

## 2 Experimental methods and theoretical background

### 2.1 Lattice defects in metals

The following chapter deals with lattice defects in metals, which play a central role in metallurgy. Defects are imperfections in the atomic arrangement. Since even in thermodynamic equilibrium defects (e. g. vacancies) are present in the crystal lattice and since a real crystal virtually never is in thermodynamic equilibrium, it always contains defects. Different types of defects are distinguished, the categorization of which is usually based on their number of dimensions: zero-dimensional (point-type) defects like vacancies and interstitial atoms, one-dimensional defects (line-type) like dislocations and two-dimensional (area-type) defects like phase or grain boundaries, twins or stacking faults. Defects considerably influence various properties of a material, that is mechanical, electrical and magnetic ones as well as processes like diffusion, recrystallization or transformations in the solid state.

**Point-type defects** A point-type defect can either be an additional or a missing atom. The additional atom might be of the same species as the host lattice atoms, which then occupies an interstitial site, or of different species (impurity atom) occupying either an interstitial site or a regular lattice site. In both cases the lattice is locally distorted due to either the accommodation of an additional atom on an interstitial site or due to differing sizes of host and impurity atoms. Moreover, combinations of these defects exist: a pair of an interstitial host metal atom and a vacancy (Frenkel defect), and a pair of anion and cation vacancies in ionically bound crystals (Schottky defect).

The formation of vacancies proceeds via diffusion of lattice atoms from the lattice interior to the lattice free surface or equivalently by diffusion of a vacancy from the sample surface to the interior. By this process the material's density decreases. Being a thermally activated defect,

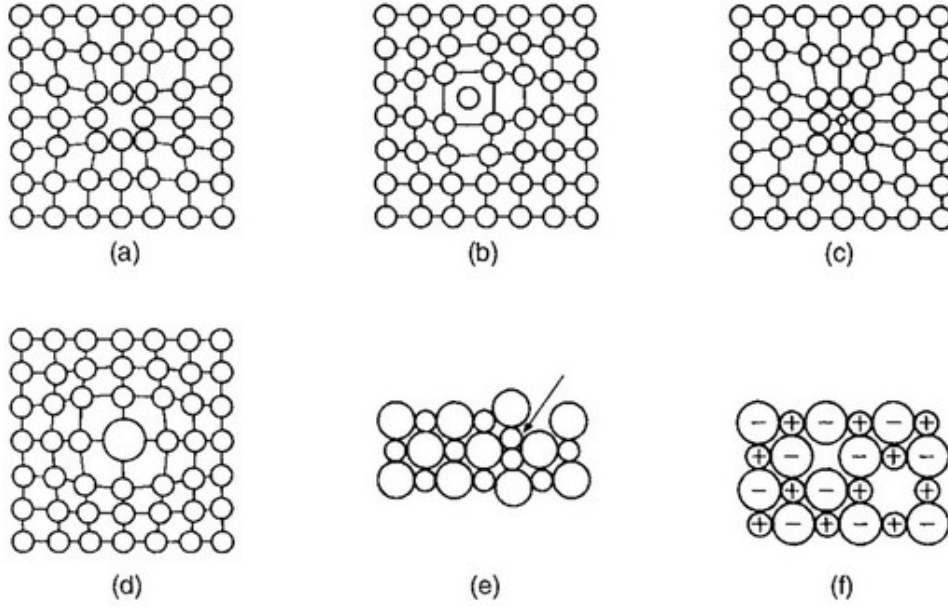


**Figure 1.** Overview of various kinds of point-type defects [28]. (a) monovacancy; (b) interstitial atom of the same type; (c) smaller and (d) larger interstitial impurity atom; (e) Frenkel defect; (f) Schottky pair

the concentration of vacancies in thermal equilibrium is given by

$$c_v(T) = e^{-\frac{g_v^f}{k_B T}} = e^{\frac{s_v}{k_B}} e^{-\frac{h_v^f}{k_B T}} \quad (1)$$

where  $g_v^f$  is the free enthalpy of formation for a vacancy,  $s_v$  the change of vibrational entropy due to formation of a vacancy and  $h_v^f$  is the enthalpy of formation for a vacancy [28], see Table 1 for experimental values.

**Table 1.** Vacancy formation enthalpy  $h_v^f$  in eV and the corresponding change in vibrational entropy  $s_v$  in multiples of Boltzmann's constant  $k_B$  for various metals [28]

		Al	Cu	Au	W	Cd
$h_v^f$	eV	0.66	1.31	0.94	3.6	0.41
$s_v$	$k_B$	0.7	2.4	0.7	2.0	0.4

Vacancies are entropically stabilized equilibrium defects and the only type of defects always present in materials. At room temperature equilibrium vacancy concentration is very small for

most metals, e. g.  $10^{-34}$  in Nb, but reaches values of approximately  $10^{-4}$  at the melting point.

**Line-type defects: Dislocations** A dislocation is an irregularity in the lattice along a line. Two types of dislocations as well as combinations of both can be found: edge dislocations (edges) and screw dislocations (screws). Edges can be illustrated by an additional lattice plane which ends somewhere in the lattice interior (Fig. 2), screws by cutting halfway through a perfect crystal then displacing one half parallel to the cut by one atomic distance.

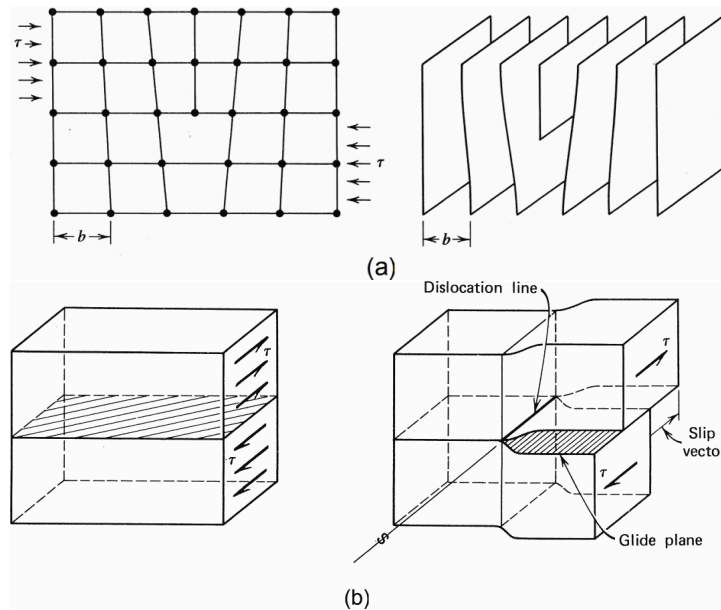


**Figure 2.** Line-type defects in a crystal [29]. (a) An edge dislocation is a lattice plane ending in the lattice interior. (b) A screw dislocation. The lattice forms a spiral around the dislocation line.

Dislocations can be described by the Burgers vector  $\mathbf{b}$  and the unit vector  $\mathbf{s}$  tangential to the dislocation line. The Burgers vector can be obtained by tracing a full cycle around the dislocation line along interatomic connection lines as a vector addition, subtracting the result of the full cycle in the defect-free state. The Burgers vector remains constant along the dislocation line, it stays perpendicular or parallel to the dislocation line for edge or screw dislocations, respectively, see Fig. 3 on p. 7.

This gives the possibility to define a dislocation's character, that is the fraction of edge ( $\mathbf{b}_e$ )

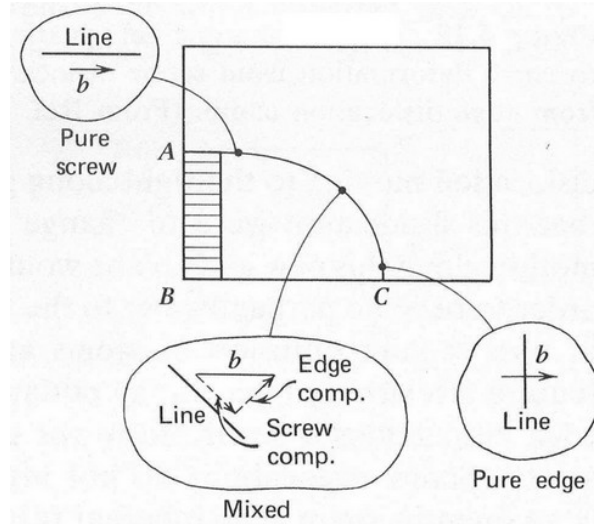


**Figure 3.** A mixed dislocation [29]. The dislocation character fades from edge to screw.

or screw ( $\mathbf{b}_s$ ) character, using the angle  $\varphi$  between dislocation line and Burgers' vector by the formulas

$$\begin{aligned}\mathbf{b}_s &= \mathbf{s} \cdot (\mathbf{b} \cdot \mathbf{s}) = (|\mathbf{b}| \cdot \cos \varphi) \cdot \mathbf{s} \\ \mathbf{b}_e &= \mathbf{s} \times (\mathbf{b} \times \mathbf{s}) = (|\mathbf{b}| \cdot \sin \varphi) \cdot \mathbf{n}\end{aligned}\quad (2)$$

where  $\mathbf{n}$  denotes the unit vector normal to the dislocation line and parallel to the additional lattice plane [28]. The great significance of dislocations is that they facilitate plastic deformation of crystalline solids. In a perfect crystal the theoretical shear stress upon which plastic deformation sets in is two to four orders of magnitudes larger than the experimentally determined value, see Table 2. This discrepancy arises from the absence of dislocations in the perfect crystal.

**Table 2.** Theoretical and experimental values of critical shear stress  $\tau_y$  for various metals [28]

		Al	Ag	Cu	Ni	$\alpha$ -Fe
$\tau_y^{th}$	GPa	0.9	1.0	1.4	2.6	2.6
$\tau_y^{exp}$	MPa	0.78	0.37	0.49	3.2	27.5

Edge dislocations move along a plane called the slip plane, the normal vector of which is

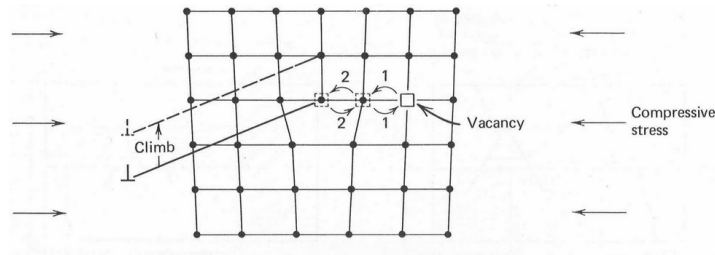


**Figure 4.** By attachment of vacancies to the dislocation core edges are able to change slip planes (climb) [29].

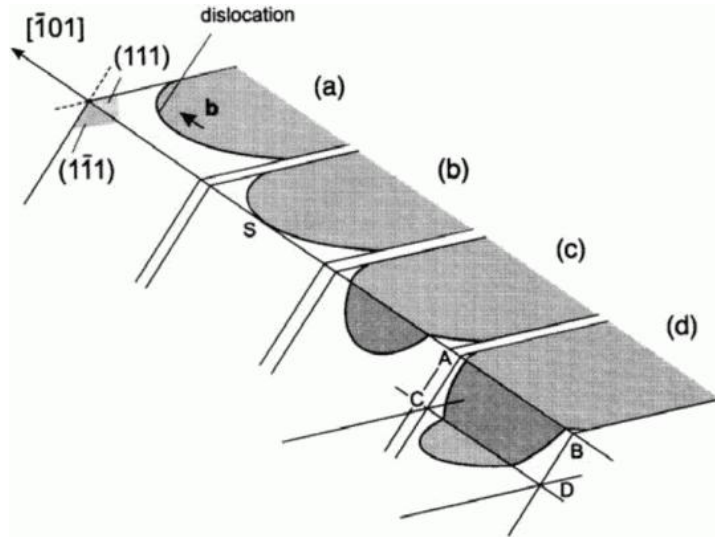


**Figure 5.** Cross slip of screw dislocations in a fcc lattice [30]

given by

$$\mathbf{m} = \mathbf{s} \times \mathbf{b}. \quad (3)$$

From (3) follows that screw dislocations do not have a well-defined slip plane ( $\mathbf{s}$  parallel to  $\mathbf{b}$ ) and thus are able to change slip planes, known as cross slip, see Fig. 5 on p. 8. Edge dislocations can change their slip planes only by climbing, Fig. 4. This process requires trapping vacancies at the dislocation core or releasing them from it.

**Area-type defects: grain and phase boundaries** A crystalline solid usually consists of many smaller crystals with varying orientation and size. If the small crystals (crystallites) are made up of the same species of atoms arranged in an identical structure they are called

grains and their interfaces grain boundaries. Phase boundaries in turn separate crystallites of different physical properties, that is phases. Grain boundaries can be classified into tilted grain boundaries and rotated grain boundaries. Tilted grain boundaries are divided into small angle grain boundaries and high angle grain boundaries. The former are caused by an array of dislocations stacked atop each other thus producing a misorientation angle between the grains. In small angle grain boundaries the grain boundary energy increases linearly with the tilt angle, but levels off as soon as dislocation cores start to overlap at a tilt angle of  $\approx 15^\circ$ . Grains boundaries with tilt angles  $> 15^\circ$  are termed high angle grain boundaries.

### 2.1.1 Vacancy formation and its consequences on density and lattice parameter

When a vacancy forms by diffusion from the lattice surface into the interior the outer volume of the body increases whereas the total mass remains constant, i. e. the density is lowered, see Fig. 6.

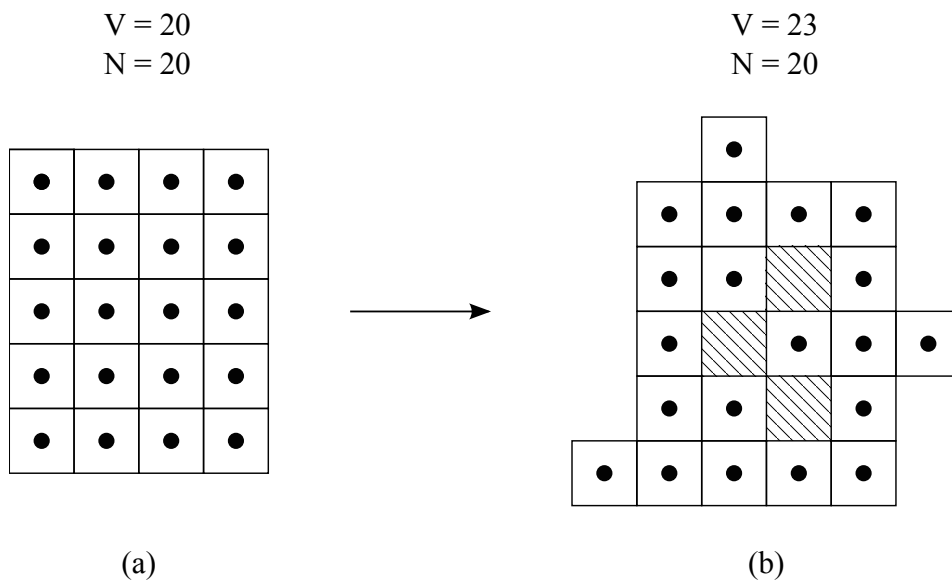


**Figure 6.** Diffusion of vacancies into the lattice interior causes an expansion in total outer volume. The density in (b) is smaller than in (a) at a constant number of atoms.

In this model the fraction of vacancies resulting from a change in density  $\Delta\rho = \rho - \rho_0$  is

calculated as

$$c_v = 1 - \frac{\rho}{\rho_0} = -\frac{\Delta\rho}{\rho_0}. \quad (4)$$

The atoms surrounding the vacancy lack the interaction with the missing atom and adopt new equilibrium positions. This relaxation results in a local contraction of the interatomic distances and hence a locally reduced lattice parameter. The contraction turns macroscopical as soon as vacancies are present in a concentration so high that the strain fields surrounding them start to overlap. Incorporating this effect into equation (4) yields

$$c_v = 1 - \frac{\rho a^3}{\rho_0 a_0^3}. \quad (5)$$

$a_0$  denotes the reference and  $a$  the reduced lattice parameter.

It has to be pointed out that the equations of vacancy concentration (4) and (5) represent values relative to a reference specimen from which  $\rho_0$  and  $a_0$  are determined. Therefore the absolute concentration of vacancies might be different.

## 2.2 Diffusion

By thermal activation atoms in a solid body are able to leave their position and move through the lattice. This process can either take place due to a concentration gradient hence establishing a homogeneous concentration profile or in a state of equilibrated concentration itself. The former process is known as chemical diffusion due to the driving force arising from inhomogeneities of the chemical potential, and the latter as intrinsic diffusion resulting from random walk. The evolution of the concentration distribution  $c(\mathbf{x}, t)$  is given by the diffusion equation (6) in case of location-independent diffusivity  $D$ .

$$\frac{\partial c(\mathbf{x}, t)}{\partial t} = D \Delta c(\mathbf{x}, t) \quad (6)$$

Speed of diffusion is mainly influenced by the potential barrier separating two equilibrium positions in the lattice, which is called activation energy  $E_a$ . The probability for an atom to move over the barrier is proportional to the exponential factor

$$\exp\left(-\frac{E_a}{k_B T}\right).$$

Hence the diffusivity can be written as an Arrhenius-type equation

$$D = D_0 \exp\left(-\frac{E_a}{k_B T}\right) \quad (7)$$

where  $D_0$  is a constant.

To estimate the distance  $\langle x^2 \rangle$  travelled by an atom into one direction as a result of random walk within a period of time  $t$  the so-called Einstein relation

$$\langle x^2 \rangle = \sqrt{2Dt} \quad (8)$$

can be utilized. For three dimensions and in case of cubic symmetry ( $\langle x^2 \rangle = \langle y^2 \rangle = \langle z^2 \rangle$ ) the Einstein relation transforms to

$$\langle R^2 \rangle = \sqrt{6Dt} \quad (9)$$

where  $\langle R^2 \rangle = \langle x^2 \rangle + \langle y^2 \rangle + \langle z^2 \rangle$ , see [31].

## 2.3 Deformation of a solid body

A solid body responds to the application of an external force by dimensional change though offers a certain resistance as opposed to gases or liquids. The deformation behaviour of a material can be characterized by hardening curves (Fig. 7) wherein external stress  $\sigma$  is plotted against (longitudinal) strain  $\varepsilon$ .

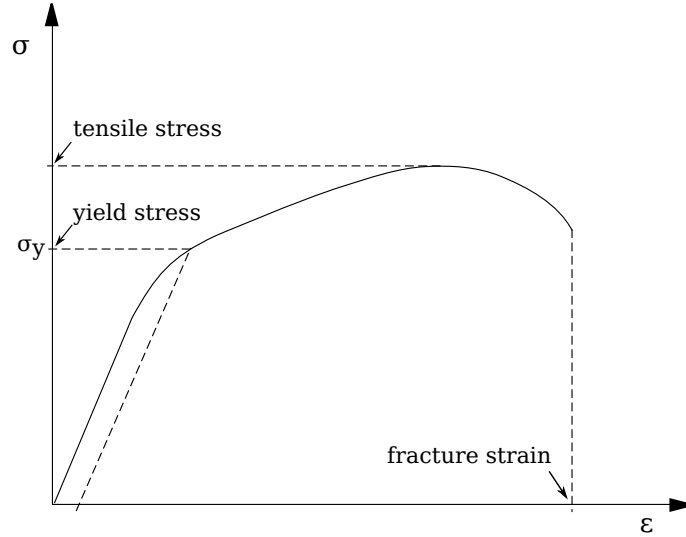


**Figure 7.** The technical stress-strain curve

### 2.3.1 The initial linear range – elastic deformation

At low strains there is usually a linear relation between stress and strain. Deformation in this section is elastic, i. e. reversible, and the stress – strain relation is given by Hooke's law for a tensile test

$$\sigma = E \varepsilon \quad (10)$$

where  $E$  is the elastic or Young's modulus. For the torsion test Hooke's law can be written with the shear modulus  $G$  correspondingly as

$$\tau = G\gamma \quad (11)$$

where  $\tau$  and  $\gamma$  is the shear stress and the shear strain, respectively. In metals this relation only holds for very small deformations (typically  $\varepsilon < 10^{-3}$ ). Upon further straining plastic deformation occurs in a ductile material, i. e. the specimen does not adopt its original dimension after releasing the external force. Furthermore the hardening coefficient  $\Theta$ , which is defined as

the hardening curve's slope

$$\Theta = \frac{d\sigma}{d\varepsilon} \quad \text{or} \quad \Theta = \frac{d\tau}{d\gamma} \quad (12)$$

becomes variable. Straining of brittle , i. e. non-ductile materials beyond the linear range quickly results in fracture and failure.

### 2.3.2 Plastic deformation

Once the external stress exceeds a certain so-called yield stress  $\sigma_y$  plastic deformation sets in. The yield stress can only be defined inaccurately because the transition from elastic to plastic deformation proceeds continuously. A widely used method is to define  $\sigma_y$  as the stress which leads to a permanent strain  $\varepsilon$  of 0.2 % after unloading.

In order for a dislocation to move in its slip system a shear force  $\tau_R$  creating a shear strain  $\gamma_R$  must act in the slip plane along the slip direction.  $\tau_R$  is called resolved shear stress and  $\gamma_R$  resolved shear strain, correspondingly.  $\sigma$  and  $\varepsilon$  represent mean values of the resolved shear stress  $\tau_R$  and the resolved shear strain  $\gamma_R$  averaged over all crystallites in a polycrystalline specimen. Schmid's law gives the relation between the macroscopic  $\sigma$  and the microscopic  $\tau$ .

$$\tau_R = \sigma \cos \kappa \cos \lambda = \sigma m \quad (13)$$

$\kappa$  and  $\lambda$  denote the angle between the effective direction of  $\sigma$  and the normal vector to the slip plane and the direction of slip, respectively. The coefficient  $m = \cos \kappa \cos \lambda$  is called Schmid-factor for which holds  $0 \leq |m| \leq 0.5$ .

Additionally to splitting the hardening curve into an elastic and plastic part, the plastic part can be divided into 5 hardening stages. Each stage is governed by different processes which influence the hardening coefficient  $\Theta$  in a characteristic way. A schematic illustration of a  $\tau$ - $\gamma$  plot in the plastic regime showing stages I–V is drawn in Fig. 9.

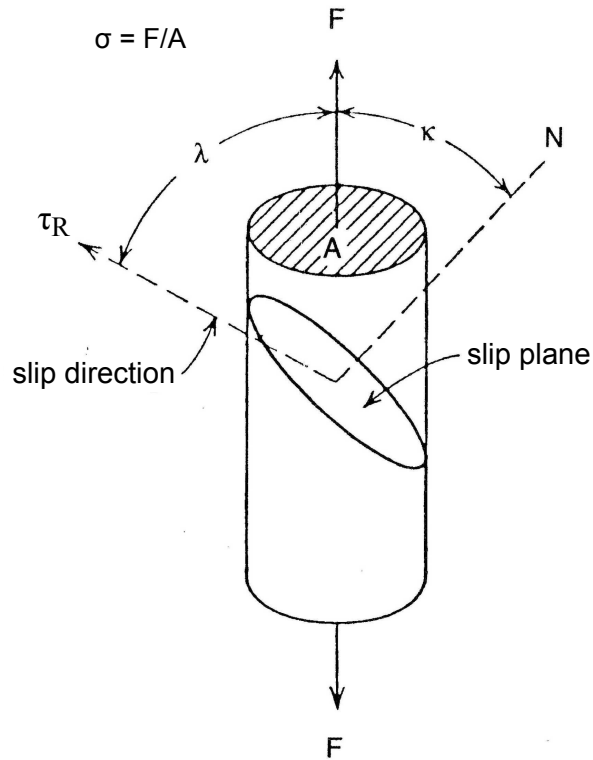


**Figure 8.** Schmid's law [28]

**Stage I:** The first stage is called easy-glide area and characterized by a small hardening coefficient. Dislocations on one slip system, that are activated for single-slip once the critical resolved shear stress is exceeded, cover long distances and run out of the material. This stage can only be found in single crystals where only one slip system is activated first.

**Stage II:** Due to blocking of dislocations as soon as  $\geq 2$  slip systems are activated locally enhanced stresses occur which allow secondary slip systems to be activated due to geometrical reasons. The newly mobilized dislocations react with such on primary slip-systems to form Lomer or Lomer-Cottrell dislocations, which are highly immobile. To maintain the imposed deformation speed new dislocations need to be introduced (e. g. at Frank-Read sources) to account for the immobilized ones. The dislocation density strongly increases. The hardening is much higher than in stage I and its value is almost

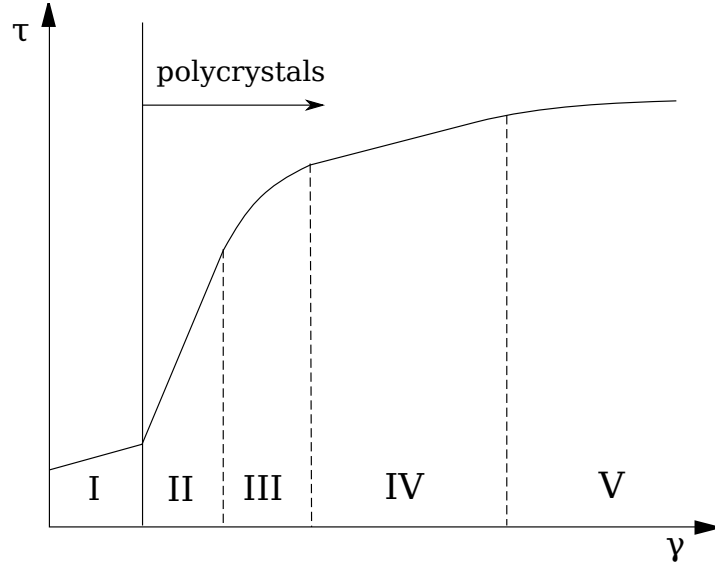


**Figure 9.** Five stages of plastic deformation in the stress-strain plot

independent of crystal orientation and structure

$$\theta_{II} \approx \frac{G}{300}$$

where  $G$  denotes the shear modulus [28].

**Stage III:** The third stage is characterized by a decreasing hardening coefficient. It is caused by cross slip of screw dislocations. In doing so screws which are blocked on a certain slip plane change to another plane with lower critical resolved stress and thus circumvent their obstacles. During this process antiparallel screws can meet and annihilate.

**Stage IV:** Screw dislocations reach dynamic equilibrium at the end of stage III; the deformation is carried again by edges and the hardening coefficient is small but persistent. The fourth stage was reported for the first time by Stüwe [32] in 1965. It is the most important stage regarding SPD since a great number of high angle grain boundaries is being formed [33, 34].

**Stage V:** In the fifth stage dynamic equilibrium is reached and the hardening approaches zero.

Dislocation formation rates balance annihilation rates, edges annihilate via climb by the assistance of deformation-induced vacancies and screws by cross-slip [33–35].

Plasticity of polycrystals differs considerably from that of single crystals, the principle difference being a higher yield strength and hardening coefficient in polycrystals. Plastic flow in polycrystals only starts when the stresses applied give rise to shear stresses exceeding the critical resolved shear stress in all grains, which needs the activation of at least 5 slip systems according to Taylor, due to the misorientation of adjacent grains. Thus stage I of plastic hardening does not occur in polycrystals.

## 2.4 Severe plastic deformation

Plastic deforming of metallic workpieces is an important means to change their properties, mainly in terms of hardness and ductility. Over the last two decades a lot of research has been done in the field of Severe Plastic Deformation (SPD) [36], where under *enhanced hydrostatic pressure at low homologous temperature* a workpiece is deformed to exceptionally high strains. SPD techniques comprise methods of metal forming which are based on the unique principle of grain refinement *without significant change* in overall geometry of the workpiece. They thus differ from more conventional methods of metal forming like rolling, extrusion or drawing. SPD techniques can be applied to a wide range of materials such as pure metals, their alloys and intermetallics [37, 38] giving rise to new and extraordinary properties, see [39] and section 2.4.1. SPD is the only method known to allow for the formation of nanocrystalline materials exhibiting crystallite sizes  $< 100$  nm immediately from the coarse grained bulk. Common to all types of SPD are the following features:

- low deformation temperature, usually below  $0.4 T_m$
- enhanced *hydrostatic* pressure
- multidirectionality of deformation

- conservation of overall workpiece dimensions
- introduction of a large number of high angle grain boundaries *and* dislocations
- refinement of grain sizes below 1  $\mu\text{m}$  down to few 10 nm
- production of *bulk* crystalline samples free from any residual porosity

Because of its specific importance to the operation of SPD the feature of hydrostatic pressure shall be stressed [40]. (i) It inhibits the formation of cracks and thus principally allows to attain arbitrarily large strain without sample failure and (ii) it hampers the movement of vacancies and hence dislocation annihilation. Moreover, it gives the possibility to deform even brittle materials, like metal hydrides, that would break during deformation by conventional techniques. Widely used SPD techniques are high pressure torsion (HPT) and equal channel angular pressing (ECAP), Fig. 10 on p. 18. For a comprehensive compilation on SPD and the fabrication of materials with crystallite sizes below 1  $\mu\text{m}$  see [1]. SPD materials are considered to have great potential for various applications in different areas of mechanical, electrical, magnetic and biomedical engineering.

Like in any plastic deformation various types of defects, like vacancies, dislocations and grain boundaries are introduced into the metal matrix during SPD.

#### **2.4.1 Paradoxon of SPD materials**

Plastic deformation induced by conventional cold working methods increases the strength of metals. However, cold work is accompanied by loss of ductility in general, causing a metal either to be strong or ductile, but not both at the same time, as seen in Fig. 11 in case of cold-rolled Cu and Al (black lines). Strengthening due to plastic deformation arises from the introduction of dislocations (dislocation strengthening), refinement in grain size (grain boundary strengthening) and misorientation of grains. Dislocations cannot move across a grain boundary, since the directions of slip given by the Burger's vector (3) are not parallel

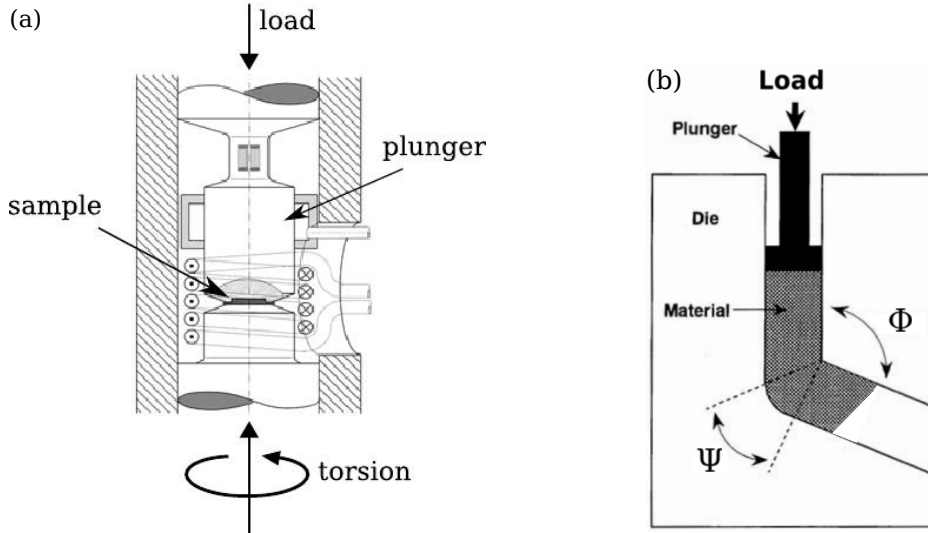


**Figure 10.** Schematic illustrations of equipments for (a) high pressure torsion (HPT) and (b) equal channel angular pressing (ECAP) [3]

for adjacent grains. Dislocation pile ups are formed at grain boundaries and generate large stresses reaching into adjacent grains, which then cause new dislocations to be introduced. The relation between yield stress  $\sigma_y$  and grain diameter  $d$  is quantitatively described by the Hall-Petch equation [41,42]

$$\sigma_y = \sigma_0 + \frac{k_y}{\sqrt{d}}. \quad (14)$$

$\sigma_0$  is the yield stress for the single crystal and  $k_y$  a constant unique to each material (Hall-Petch strengthening coefficient). An extraordinary feature of SPD processed materials is the combination of both high strength and high ductility, as seen in Fig. 11 for Ti and Cu. In addition to creating a nanosized structure, the SPD process mainly causes the formation of a large number of dislocations. In contrast, conventional forming methods such as rolling to small strains mainly introduce low-angle grain boundaries. In coarse grained materials the primary mechanisms underlying plastic flow are dislocation movement and twinning. High-angle grain boundaries in ultra-fine grained metals form effective impediments for dislocations thus enhancing strength. Furthermore, grains smaller than  $\approx 20$  nm undergo other yielding mechanisms, like grain boundary sliding and grain rotation, which in turn increase ductility.

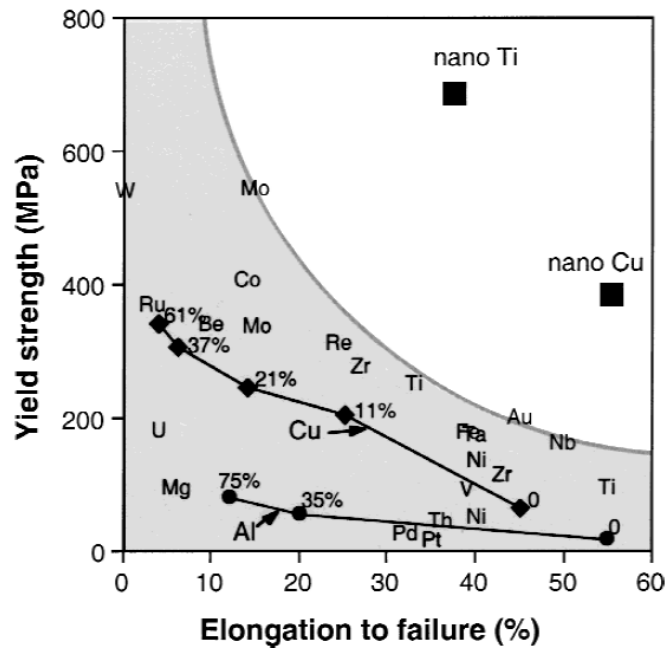


**Figure 11.** Cold rolling of Cu and Al increases yield strength but simultaneously reduces elongation to failure, that is ductility. (At each data point reduction in thickness is noted.) Nanocrystalline Ti and Cu processed by SPD exhibit a remarkable combination of both features [43].

#### 2.4.2 High pressure torsion (HPT)

Torsion tests represent a major tool in studying high strains; the highest plastic strains so far have been reached by HPT. During HPT a disk-shaped sample is placed into a cavity between two anvils upon which high pressure is then applied. The anvils convey the load onto the sample and produce hydrostatic pressure – usually on the order of few GPa – in the sample. The anvils are then rotated against each other and, in this way, they enforce a torsional deformation upon the sample by pure shear forces. Figure 10a schematically depicts the general set-up of an HPT device. Assuming the absence of outward material flow due to perfect sealing of the sample

cavity<sup>1</sup>, the deformation grade is given by the torsional strain

$$\gamma = 2\pi N \frac{r^{\star}}{d} \quad (15)$$

where  $r^{\star} = 2r/3$ ,  $r$  denotes the sample radius and  $d$  its thickness after HPT. The equivalent strain for torsional deformation can be calculated as [45]

$$\varepsilon = \frac{\gamma}{\sqrt{3}}. \quad (16)$$

Due to the continuous deformation without interruption or change of path, in principle, an infinite grade of deformation can be achieved by one single path in HPT. Grain sizes in alloys after HPT usually range from 70 to 500 nm.

## 2.5 Hydrogen in metals

Hydrogen (H) is the simplest and smallest of all atoms – consisting of one proton and one electron – and the most abundant element in the universe. Having the atomic number 1 it is the lightest element with standard atomic weight of 1.00794(7) u . It can be either regarded belonging to the elements in the first (alkaline metals) or 17<sup>th</sup> group (halogenes) in the periodic system of elements. At room temperature and standard pressure H forms the diatomic molecular gas H<sub>2</sub> with a density of  $8.988 \cdot 10^{-5} \text{ g cm}^{-3}$ . Many metals and alloys are capable of absorbing H. The absorption of hydrogen from the gaseous phase by metals was first observed in 1867 by T. Graham for palladium (Pd) [46]. In the host-metal lattice H atoms occupy interstitial sites (interstices). Figure 12 shows the positions and Table 3 the number of octahedral (O) and tetrahedral (T) interstitial sites in fcc, bcc and hcp lattices, respectively.

In general, at low concentrations H atoms are randomly distributed over interstices but at

---

<sup>1</sup>This is a simplification because in a real HPT-device sample material will be pressed out of the cavity at the start of the deformation process and hence the sample thickness will be reduced. For a more rigorous treatment see [44]. However, this is of minor importance for measurements conducted in the course of the present work and will hence be neglected.

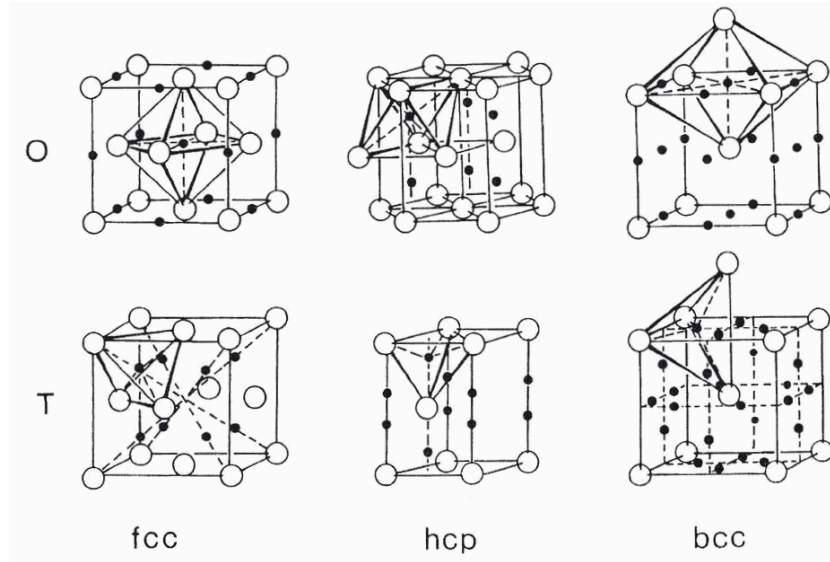


**Figure 12.** H atoms on interstitial octahedral (O) and tetrahedral (T) sites in fcc, bcc and hcp lattices. The host-metal atoms are marked as open circles; the H atoms as small dots. Taken from [19]

**Table 3.** Number of interstitial sites per host-lattice atom

type	fcc	hcp	bcc
O	1	1	3
T	2	2	6

higher concentrations, when H – H interactions come into play, H-ordered phases appear. It is customary to denote the H content by  $x = [\text{H}]/[\text{M}]$ , i. e. the atomic ratio of H atoms to M atoms.

The absorption process of gaseous  $\text{H}_2$  into a host-metal lattice can be divided into four steps [47]:

1. adsorption of molecular  $\text{H}_2$  onto the metal surface by van der Waals forces (physisorption)
2. dissociation of  $\text{H}_2$  molecules into single H atoms
3. chemisorption of single H atoms
4. diffusion into the lattice interior via interstitial hopping

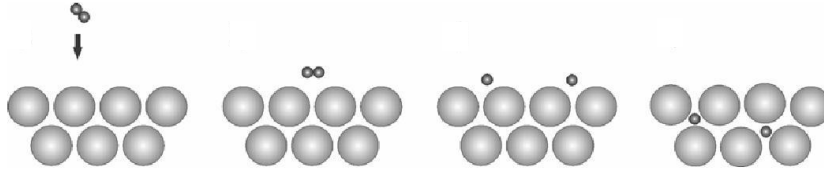


**Figure 13.** Absorption process of molecular  $H_2$  onto interstitial host-lattice sites [48]

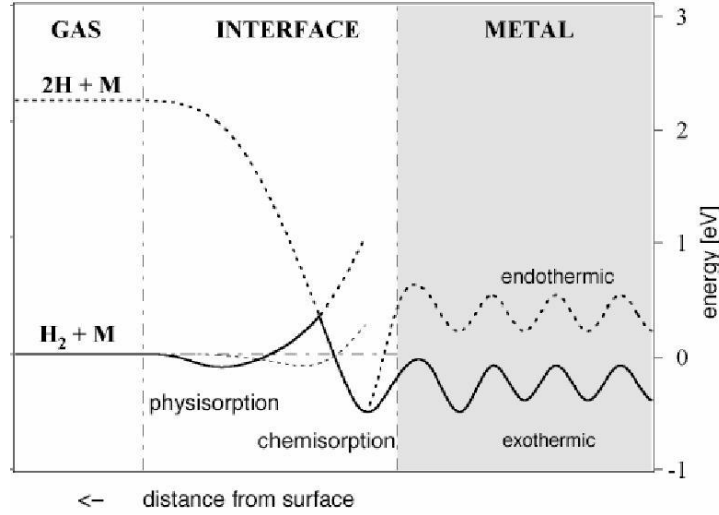
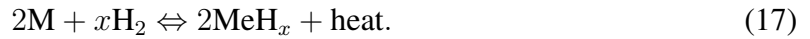


**Figure 14.** Potential line for  $H_2$  molecule and single H atom around the metal surface [48]

Every partial process proceeds with its own rate, the step of dissociation being often the slowest and thus rate-limiting.

In the low concentration regime gaseous  $H_2$  reacts with a metal according to



In most cases the process of H absorption is exothermic, thus releases heat, and accordingly H desorption mostly is endothermic, hence requires supply of heat. The chemical potential of H dissolved in the metal is given by

$$\mu_H = \mu_H^\circ + RT \ln \frac{n}{1-n} + \Delta\mu_H \quad (18)$$

where  $\mu_H^\circ$  denotes the standard chemical potential. The second term on the right hand side

comprises the configurational entropy for ideal statistical distribution of H atoms among interstitial sites, where  $n = [\text{H}]/N_s$  and  $N_s$  denotes the total number of interstitial sites. In case of fcc Pd first O-sites become occupied by H atoms upon loading and since the number of O-sites equals the number of Pd atoms ( $[\text{Pd}]/N_o = 1$ ) the configurational entropy can also be written as

$$R \ln \frac{x}{1-x} \quad (19)$$

for low concentrations of H. The last term  $\Delta\mu_H$ , often called excess term, contains contributions which cause deviation from the ideal solid solution behaviour. Thermal equilibrium of (17) is attained when the chemical potential of H in the gaseous phase equals the chemical potential of H in the metal.

$$\mu_H = \frac{1}{2}\mu_{H_2} = \frac{1}{2}\mu_{H_2}^\circ + \frac{1}{2}RT \ln p_{H_2} \quad (20)$$

By omitting the last term in (18) in the case of the ideal low-concentration solid solution and combined with (20) one obtains

$$\sqrt{p_{H_2}} = \exp\left(\frac{\mu_H^\circ - 1/2\mu_{H_2}^\circ}{RT}\right) \cdot \frac{x}{1-x} = K \cdot \frac{x}{1-x}. \quad (21)$$

For  $x < 0.05$  the fraction on the right side can be approximated by the atomic concentration  $c_H$  of H.

$$\sqrt{p_{H_2}} = K \cdot c_H \quad (22)$$

This relation is called Sieverts' law<sup>2</sup> and the exponential factor, abbreviated to  $K$ , accordingly Sieverts' constant; it was reported already in 1929 [49]. It states that for an ideal M-H solution in thermal equilibrium with gaseous  $\text{H}_2$  the amount of H present in the metal in the low-concentration regime is proportional to the square root of the H pressure in the gaseous phase. Relation (21) was derived for the dissolution of a *diatomic* gas which dissociates upon absorption. For an n-atomic gas the reaction can be described by  $\sqrt[n]{p}$  correspondingly.

---

<sup>2</sup>Adolf Sieverts, born 1874 in Hamburg – died 1947 in Jena

At low H-concentration a solid solution is formed, i. e. the H atoms are dissolved on interstitial sites in the host-metal lattice structure native at the corresponding temperature. By increasing the H content at constant temperature the  $H_2$  equilibrium-pressure increases, see the  $\alpha$ -phase region in Fig. 15b. Once a certain solubility limit is crossed the isotherm enters a miscibility gap and a new phase, the so-called hydride phase starts to nucleate and grow (denoted with  $\beta$  in Fig. 15b). The hydride phase can be of a different lattice structure than the solid solution  $\alpha$ -phase or of the same exhibiting a larger unit cell thereby creating a lattice mismatch between the  $\alpha$  and the  $\beta$ -phase. This mismatch leads to the development of internal stresses which can cause deformation and introduction of defects. In contrast to single-phase regions the H equilibrium-pressure stays roughly constant along the isotherm in the two-phase region, where  $\alpha$  and  $\beta$ -phases coexist. By increasing the H content in the miscibility gap (two-phase region) the newly forming hydride phase consumes the low-concentration solid solution until the so-called terminal solubility limit where all  $\alpha$ -phase is converted to  $\beta$ -phase. From there on the H equilibrium-pressure rises again.

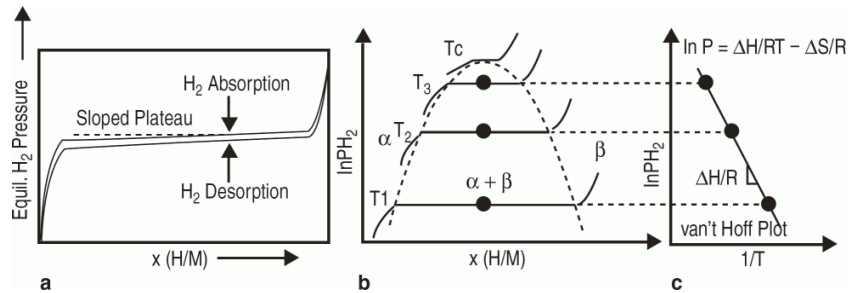


**Figure 15.** (a) The difference in  $H_2$  equilibrium-pressure upon absorption and desorption leads to a hysteresis. (b) A Pressure-Composition-Temperature (PCT) diagram. The left and the right boundary of the central area, where the  $\alpha$  and the  $\beta$ -phase coexist, represent the solubility limit and the terminal solubility limit, respectively. (c) Construction of a van't Hoff plot to extract the enthalpy  $\Delta H$  and entropy  $\Delta S$  of hydride formation. Taken from [50]

Turning to higher temperatures the plateau decreases in length and finally vanishes at a critical temperature above which the loading proceeds continuously, i. e. without separation into a low and a high H-concentration phase.

By plotting the logarithm of the plateau pressure over  $1/T$  ( $T$  the temperature of the corresponding isotherm) the enthalpy  $\Delta H$  and entropy  $\Delta S$  of hydride formation can be extracted according to

$$\ln(p(T)) = \frac{\Delta H}{RT} - \frac{\Delta S}{R}. \quad (23)$$

This relation is called van't Hoff equation and its application is shown in Fig. 15c. Plateau pressures upon absorption and desorption of H differ slightly, the former lying usually at higher values than the latter, see Fig. 15a. This phenomenon is called hysteresis and attributed to the lattice misfit between the two phases found at both sides of the two-phase region.

The accommodation of H into the crystal lattice of the host metal causes the lattice to expand. Each H atom brings about a displacement of the surrounding lattice atoms from their regular sites. Thereby the lattice is distorted and local internal stresses develop. Due to inhomogeneous expansion during loading via a two-phase region, a large number of dislocations will be formed, once the yield stress is exceeded. This can eventually cause pulverization of bulk samples. Typical relative volume expansion due to solution of one H atom per metal atom is as high as 20 %.

The term hydride is rather loosely defined and usually describes either a phase of high H-concentration, or a M-H system close to or at stoichiometric composition, like PdH or TiH<sub>2</sub>.

The composition and the structure of a M-H system in thermodynamic equilibrium can be presented by means of Temperature-Composition (TC) phase diagrams (Figs. 16 on p. 27 and 17 on p. 28) and Pressure-Composition-Temperature (PCT) diagrams (Figs. 15b, 26 on p. 46 and 29 on p. 49), where in the former the temperature and in the latter the H equilibrium-pressure is plotted over the composition, respectively. PCT-diagrams are of big importance in carrying out hydrogenation.

Since all metals, except Pd, have an even greater affinity for oxygen than for hydrogen the surface of specimens is usually coated with an oxidized layer, which inhibits the uptake of H. This layer can be removed or broken by heating the sample or temperature cycling in H.

atmosphere, respectively, which is called activation.

Heavier isotopes of H in metals behave similarly to protium, however, changes in thermodynamics and kinetics, have been observed. These changes result in shifts of phase boundaries and altering of diffusion rates due to higher masses.

### 2.5.1 The palladium-hydrogen system

Palladium (Pd) is a group 10, 4d transition metal with atomic number 41 and standard atomic weight 106.42(1) u. Its lattice structure is fcc with a lattice parameter of 0.389 nm.

Since T. Graham's discovery of H absorption in Pd [46], palladium hydride (PdH) is used as a model system for the investigation of hydrogen behaviour and hydrogen related properties in metals. Pd readily absorbs H so that in general no activation is necessary to enable H uptake. Therefore, PdH is the most extensively studied of all metal hydrides.

The Pd-H system exhibits a fairly simple phase diagram (Fig. 16) showing a broad miscibility gap in the lower concentration range below 571 K. At 0 K the gap extends over  $0 \leq x \leq 0.63$  approximately. Another, yet small, two-phase region can be found at temperatures below 90 K at in a concentration range between around  $0.7 \leq x \leq 0.95$ .

Both the low-concentration  $\alpha$ - and high-concentration  $\beta$ -phase are solid solutions arranged in a fcc structure where H atoms occupy O-sites. In both phases distribution of H atoms is disordered [47], in contrast to the low-temperature phases where the H atoms attain an ordered state. The O-sites themselves form a fcc lattice shifted by  $a/2$  relative to the Pd lattice along one coordinate axis. For a concentration of  $x = 1$  all O-sites are occupied.<sup>3</sup> During H absorption the lattice expands isotropically, the volume change per unit cell volume  $\Omega$  and unit concentration H in Pd is [20]

$$\Delta v/\Omega = 0.19 \pm 0.01$$

Expansion caused by uptake of D is about 5 % larger than for H. Diffusion occurs via interstitial

---

<sup>3</sup>If – instead of octahedral – all tetrahedral sites were occupied, the concentration would be 2, because 2 tetrahedral sites exist per host lattice fcc atom.

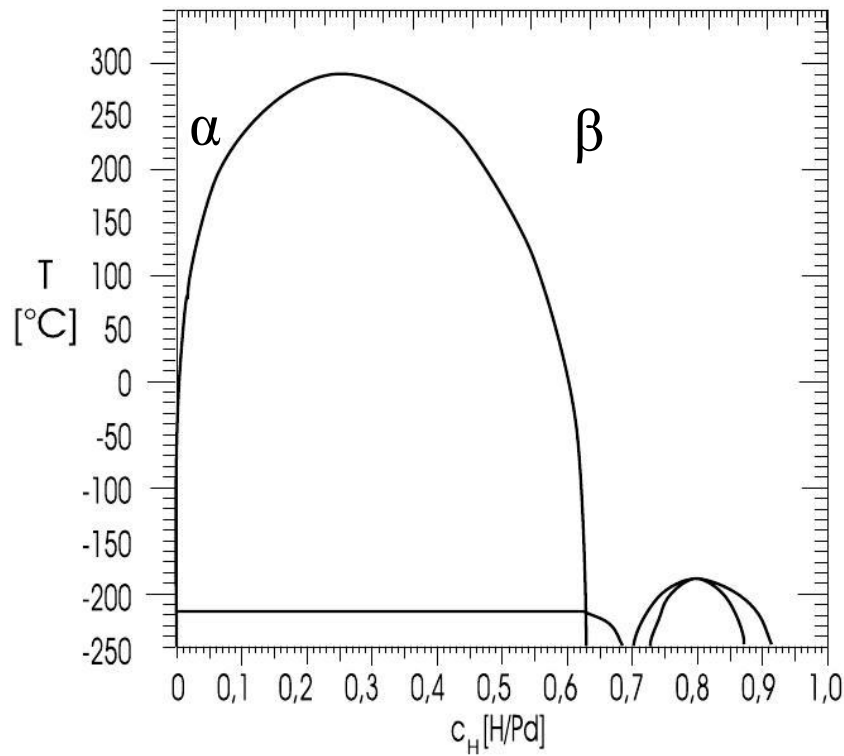


**Figure 16.** Temperature-composition phase diagram for the Pd-H system [51]. In both the  $\alpha$ - and the high-concentration  $\beta$ -phase H is distributed randomly over the interstices. See Fig. 26 for the PCT-diagram.

hopping between O-sites. The transition between the O-sites proceeds not in the direct line but over T-sites. The intrinsic diffusivity for H in Pd at low concentrations at room temperature is large –  $D = 3.97 \cdot 10^{-7} \text{ cm}^2\text{s}^{-1}$  – compared to other fcc metals, e. g. Cu and Ni. Values for  $D_0$ , diffusivity at 0 K, and the activation energy  $E_a$  are  $2.9 \cdot 10^{-3} \text{ cm}^2\text{s}^{-1}$  and 0.23 eV, respectively [22].

### 2.5.2 The titanium-hydrogen system

Titanium (Ti) is a 4<sup>th</sup> group transition metal with atomic number 22 and standard atomic weight 47.867(1) u. It is a lightweight ( $\rho = 4507 \text{ kg m}^{-3}$ ), corrosion and temperature resistant white-silvery element. Pure Ti exists in two lattice modifications, as hexagonal close packed  $\alpha$ -Ti between 0 K and 1155 K, and as body centered cubic  $\beta$ -Ti at higher temperatures up to the melting point at 1941 K. Figure 17 shows the phase diagram of the Ti-H system, which

is of an eutectoid type. Two hydride phases have been observed so far: fcc  $\delta$ -TiH and the tetragonally face-centered (fct)  $\varepsilon$ -TiH, which are among the hydrides of highest H density, with  $9 \cdot 10^{22}$  H atoms per  $\text{cm}^3$  in titaniumdihydride ( $\text{TiH}_2$ ) [52]. In both the  $\delta$  and  $\varepsilon$ -phase hydrogens are randomly distributed over tetrahedral interstitial sites except for the stoichiometric  $\text{TiH}_2$  where all O-sites are filled. At low temperatures around a concentration  $x \sim 2$  (66 at%), which corresponds to the limiting case of all T-sites filled up with H atoms,  $\delta$ -TiH transforms into the tetragonal variant. The solubility of H in the  $\alpha$ -phase is rather small, therefore precipitates of hydrides soon form upon hydriding below 300 °C [53].

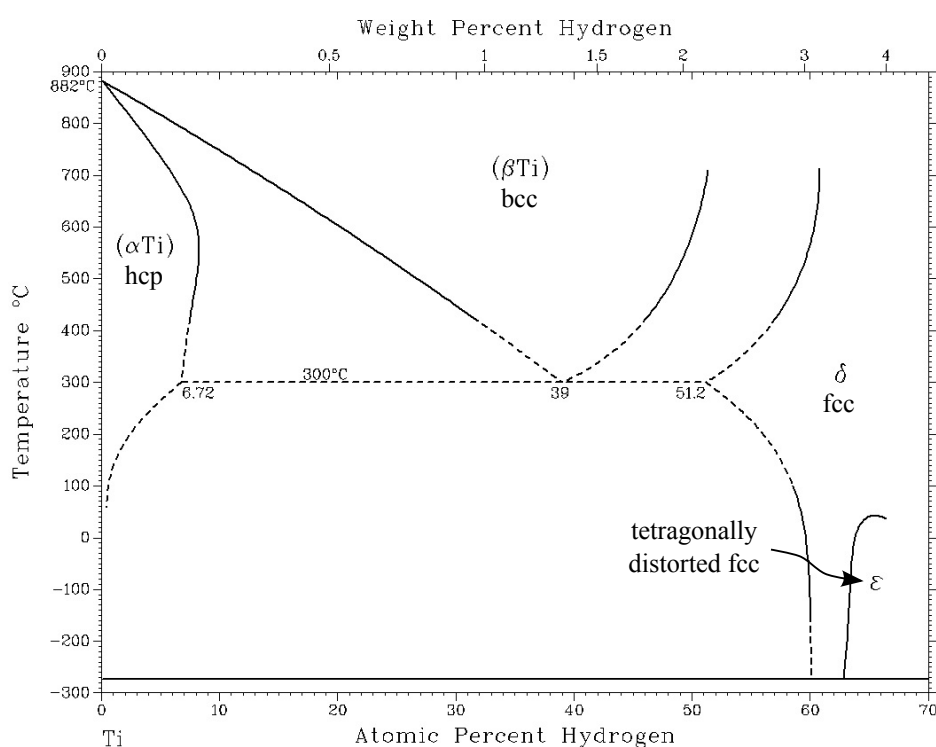


**Figure 17.** Temperature-composition phase diagram for the Ti-H system [27].

### 2.5.3 Diffusion of interstitial hydrogen in metals

Interstitally dissolved hydrogen atoms in a host-metal lattice “are the realization of a diffusing lattice gas. The host-metal atoms can be considered as immobile whereas the H atoms can diffuse on their interstitial sublattice” [54].

Hydrogen atoms can move exceptionally fast through a host-metal lattice by jumping on interstitial sites, reaching jump rates up to  $2 \cdot 10^{12}$  at room temperature in case of vanadium (V). Its diffusivity is many orders of magnitude larger than for other common interstitial elements<sup>4</sup> and comparable to the value typical for atomic diffusion in liquids, that is  $2.6 \cdot 10^{-5}$  for molecular diffusion of water at room temperature. The high mobility is a consequence of H's low mass and small size, resulting in a low activation energy for diffusion. The lowest activation energies can be found in bcc-structured metals (e. g. 0.05 eV for diffusion of H in V). Besides via classical diffusion H can move by quantum-mechanical tunneling. Tunneling processes dominate at low temperatures causing higher diffusivities compared to classical diffusion systems. The tunneling proceeds without phonons (zero-phonon processes) in the extremely-low-temperature regime and by the assistance of one, few or many phonons as the temperature is raised (phonon-assisted processes). At still higher temperatures diffusion is dominated by the classical over-barrier jump process. A detailed description of the predominant diffusion processes in dependence of temperature regimes can be found in [19].

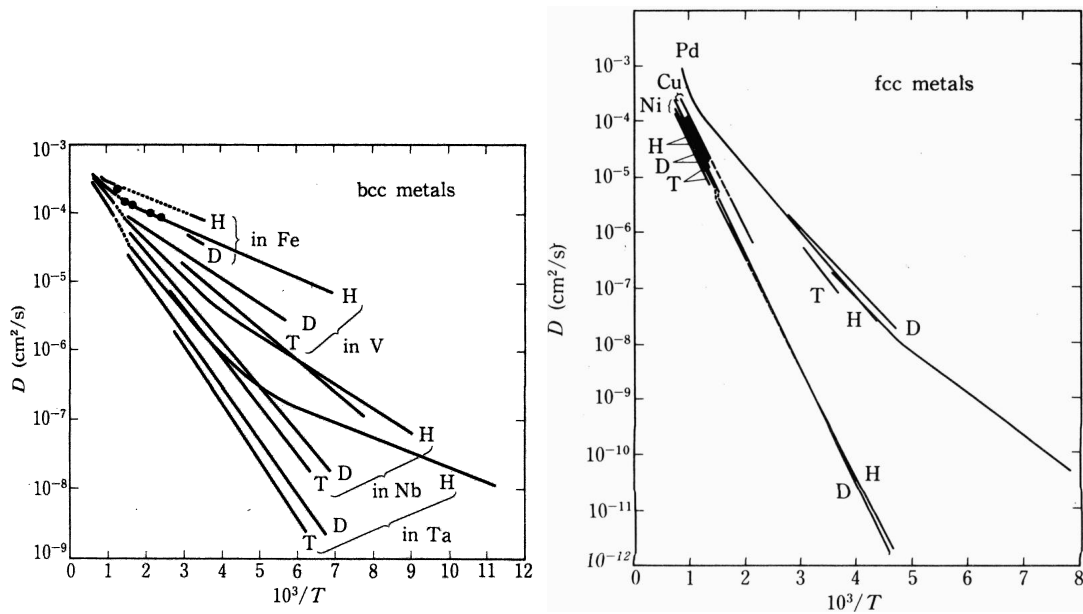


**Figure 18.** Diffusivities of H isotopes in various bcc and fcc metals [19].

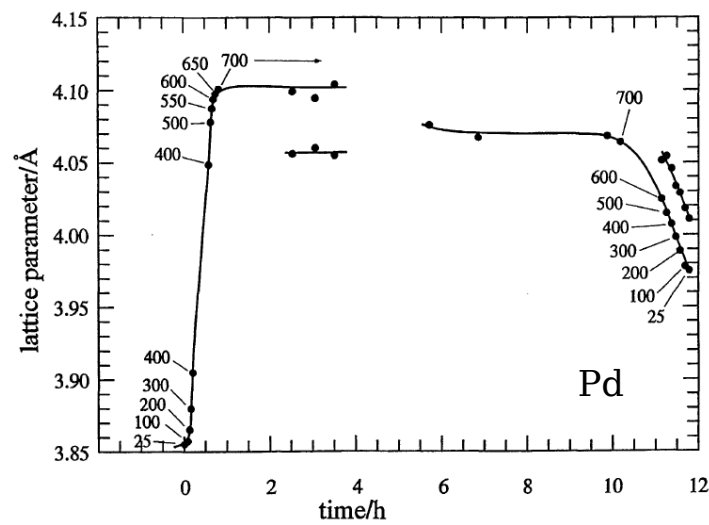
<sup>4</sup>In case of carbon the difference at 300K is around 15 (!) orders of magnitudes.

Figure 18 shows the diffusivities of H and its isotopes in the bcc metals iron (Fe), vanadium (V), niobium (Nb) and tantalum (Ta).

In case of tantalum the diffusivity of H at 90 K still is as high as  $10^{-8} \text{ m}^2 \text{ s}^{-1}$ .

#### 2.5.4 Fukai's concept of superabundant vacancies (SAVs)

In 1993 Y. Fukai et al. [8] observed a decrease in lattice parameters during *in-situ* X-ray measurements on Ni- and Pd hydride, when holding a specimen under high H pressure of 5 GPa and elevated temperature between 700–800 °C for several hours, see Fig. 19.



**Figure 19.** Evolution of lattice parameter in Pd held under high  $\text{H}_2$ -pressure of 5 GPa. The course of temperature is inscribed in °C. [8]

The lattice contraction amounted up to  $\sim 1.5\%$  and was conserved after degassing the sample of hydrogen and returning to ambient pressure and temperature. Densities measured afterwards on these samples were found to be lower than that of untreated samples. The only possibility to accommodate both changes, i. e. contraction of lattice parameters and reduction in density at the same time is the formation of vacancies or voids inside the metal lattice. Values for the corresponding vacancy concentrations of up to 20 at% were calculated. The vacancy

concentration  $c_v$  in atomic percent was calculated as

$$c_v = -\Delta\rho/\rho_0 - 3\Delta a/a_0 \quad (24)$$

where  $\Delta\rho = \rho - \rho_0$  and  $\Delta a = a_0 - a$  are changes in density and lattice parameter, respectively, with respect to their original values  $\rho_0$  and  $a_0$ , see [55].

Vacancies existing on this order of magnitude are in a supersaturated state compared to vacancies introduced by pure thermal excitation. Hence the adoption of some kind of ordered structure by these vacancies at low temperatures was assumed. In fact, X-ray diffraction analysis of Pd samples showed two coexisting phases, the first being nearly stoichiometric PdH with fcc structure and the second being fcc as well but exhibiting a smaller lattice parameter and showing superlattice reflections having simple-cubic indices (100), (110), (210), and (211) [9]. The arrangement proposed for this phase is a fcc lattice on which one of the four simple-cubic sublattices is occupied by vacancies. It is of the  $\text{Cu}_3\text{Au}$  type and can be written as  $\text{Pd}_3\text{VacH}_n$  correspondingly. So far vacancy-ordered phases could be observed in the hydrides of Pd, PdRh alloys [56] and Ni [57]. Formation of such a phase results in an increase in H solubility, the degree of which depends on the number of H atoms that can cluster at a monovacancy. In this case the H concentration is given by  $x = n/3$ , since for every three Pd atoms  $n$  H atoms are present, according to the chemical formula  $\text{Pd}_3\text{VacH}_n$ . The superlattice reflections vanish almost discontinuously above a certain temperature suggesting this order-disorder transition to be of first order [9]. The same transition can be observed on the ordered  $\text{Cu}_3\text{Au}$  system during heating.

When specimens are subjected to adequate heat treatment, after H-induced vacancies have been produced, pores 20–200 nm in size can be observed at the sample free surface and as well inside the bulk. It is thought that they are formed by vacancies which agglomerated during heat treatment. SEM studies revealed that the voids were larger in size in regions near the sample surface compared to the sample interior. Further, samples heated for shorter times

during vacancy formation showed less and smaller voids in the sample interior. This shows that these voids are formed by vacancies which diffused from the sample surface to the interior [57].

It is known that a single vacancy in Pd can trap up to at least six H atoms or H couples [58]. This number corresponds to the six octahedral sites around a vacancy in both fcc and bcc lattices. Following from the fact that aforementioned vacancy concentrations are far above thermal equilibrium at room temperature the formation energy for a vacancy must be decreased due to the attachment of H atoms. The formation energy for a single vacancy  $e_v^f$  is then lowered by the binding energies of H atoms trapped at the vacancy, the total formation energy of the resulting vacancy-H (Vac-H) cluster can be written as

$$e_{cl}^f = e_v^f - \sum_i n_i e_i^b \quad (25)$$

$e_i^b$  and  $n_i$  denote the binding energies and the number of corresponding H atoms, respectively. Two different binding energies can be distinguished,  $e_1^b$  and  $e_2^b$ . The binding energy for the first two trapped atoms  $e_1^b$  is slightly larger than the corresponding value for the third to sixth atoms. Table 4 gives a compilation of this values for selected metals. Thus, in case of Pd the formation energy of a vacancy is reduced from 1.7 eV to  $1.7 - 2 \times 0.23 - 4 \times 0.15 = 0.64$  eV.

**Table 4.** Binding energies in eV of H atoms to monovacancies in various metals [19]

metal	$e_1^b$	$e_2^b$
Al	0.52	
Ni	0.44	0.28
Cu	0.42	0.22
Pd	0.23	0.15
Fe	0.63	0.43
Zr	0.28	
Mo	1.08	
Ta	0.42	

The formation of SAVs provides an explanation for the following features observed:

- In Ni, Pd and their alloys a discontinuity in the lattice expansion induced by absorption of H can be seen [8]. Upon absorption of H the atomic volume first increases at a rate of  $\sim 2.8 \text{ \AA}^3$  per H atom up to a concentration of  $x \sim 0.7$  but levels off afterwards. This decrease in slope can be understood by the transition to the ordered  $M_3\text{VacH}_n$  structure, which exhibits a higher H solubility than the normal interstitial fcc solid solution.

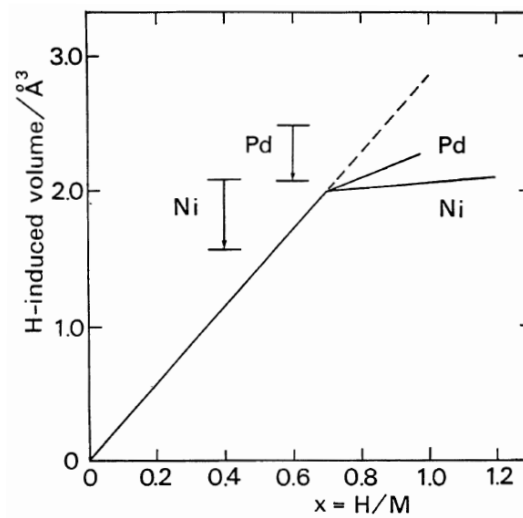


**Figure 20.** H-induced lattice expansion in Ni and Pd. The vertical bars give the difference in initial and final value before and after the heat treatment. [8]

- The feature of enhanced diffusivity of host metal lattice atoms for some Pd alloys in H-atmosphere, known as Hydrogen-Induced Lattice Mobility (HILM) can also be explained in terms of formation of a great number of vacancies. Since the self-diffusivity of lattice atoms is directly proportional to the vacancy concentration by assuming vacancy concentrations of  $10^{-17}$  at  $600^\circ\text{C}$  and  $10^{-3}$  for H-induced ones at room temperature, the self-diffusivity is  $10^{14}$  times greater in case of presence of H-induced vacancies.
- Furthermore an increase in melting point of PdH containing high concentrations of vacancies could be observed [9]. Usually the melting point of pure metals is decreased by vacancies. Whereas the PdH devoid of copious vacancies melted slightly above  $800^\circ\text{C}$

at a  $H_2$ -pressure of 5 GPa, the vacancy containing variant retained its crystalline state at the same temperature.

The fact that the defect-rich hydride phase produced at elevated temperatures and high H-pressures is retained after cooling and unloading implies that this particular defectuous phase is in fact thermodynamically more stable than the defect-free system. Speaking thermodynamically, the defect phase exhibits a lower Gibbs free energy than the non-defect one. During ordinary H-loading techniques like absorption from the gas phase (Sieverts' method) or electrolysis Vac-H clusters cannot form because temperatures are too low to enable sufficiently high diffusive flow of host lattice vacancies from the surface into the sample interior. Hence, according to Y. Fukai, the phases reported so far in M-H phase diagrams (under low temperatures and pressures) can be considered to be metastable and do not represent the system's absolute energetic minimum.

### **2.5.5 Formation of SAVs in PdH generated by HPT**

Observations presented in [16] provided for the first time evidence for the formation of SAVs in PdH during HPT at low homologous temperature. Samples of Pd in the pure state and with samples of Pd hydrogenated up to a concentration of  $x = 0.78$  were deformed by HPT at a pressure of 8 GPa and temperature of 220–265 K to different equivalent strains. After depositing the deformed samples of  $PdH_{0.78}$  for two months at RT to allow for desorption of interstitial H DSC was carried out, see Fig. 21. The peaks at around 330 K and between 480–590 K in pure HPT-Pd could be attributed to the annealing of mono-vacancies, and processes of recovery and recrystallization, respectively, by comparison with literature [59]. Using the formation enthalpy for one mono-vacancy of 1.7 eV [19] a corresponding concentration of mono-vacancies of  $6.5 \cdot 10^{-5}$  was deduced from the total energy released. In both hydrogenated samples a new sharp exothermic peak at 482 K was found, which was not observed in pure HPT-processed Pd. In-situ TEM investigations during heating permitted to relate this peak to the annealing

of point-type defects and the peak between 535 K and 750 K to recovery and recrystallization processes coupled to the rearrangement and annealing of dislocations and grain boundaries [16]. A single vacancy in an fcc lattice like Pd can trap up to 6 H atoms, displaced from the vacancy center towards the adjacent octrahedral interstices [58,60]. By ascribing the peak at 482 K to the dissociation of such Vac-H<sub>6</sub> clusters, a vacancy concentration of  $6.5 \cdot 10^{-4}$  was calculated from total peak energies in both hydrogenated samples [16]. This value exceeds by one order of magnitude the concentration of mono-vacancies in pure hydrogen-free HPT-processed Pd.

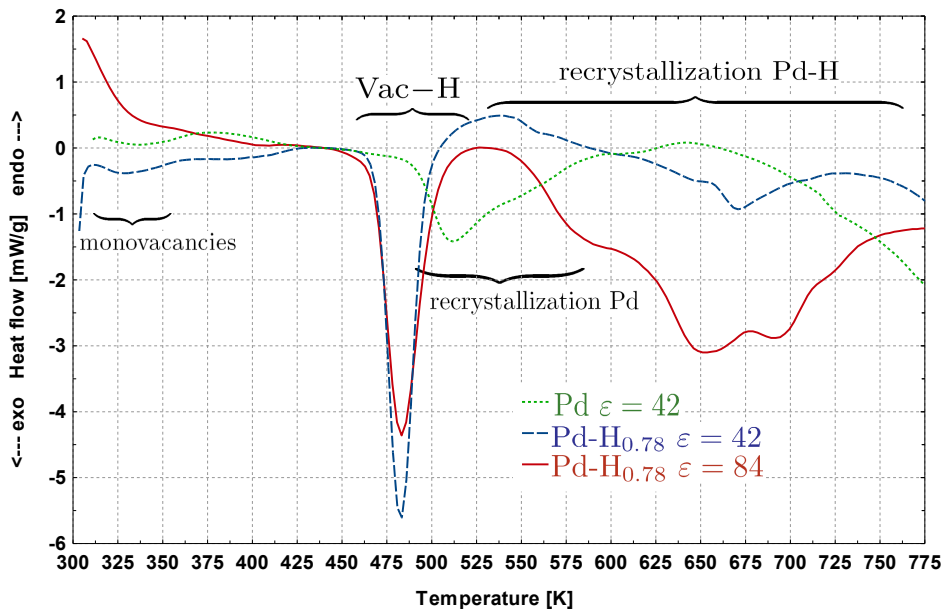


**Figure 21.** DSC-graphs for pure and hydrogenated Pd deformed to different equivalent strains  $\varepsilon$  by HPT at a low homologous temperature of  $\approx 0.15 T_m$  (220–265 K) and 8 GPa [16]

The peak ascribed to the dissociation of the Vac-H clusters is found to occur at a temperature of 482 K, hence shifted to higher temperatures by more than 140 K relative to the annealing peak of mono-vacancies. Additionally, in hydrogenated HPT-deformed Pd the onset temperature of recovery and recrystallization, i. e. of the annealing of dislocations and/or grain boundaries is shifted to higher temperatures by about 50 K. It was concluded that stabilization by excess H may occur not only for vacancy-type defects but also for other deformation-induced defects

like dislocations and grain boundaries, and that “nanometals may experience a marked increase in thermal stability through solute hydrogen.”

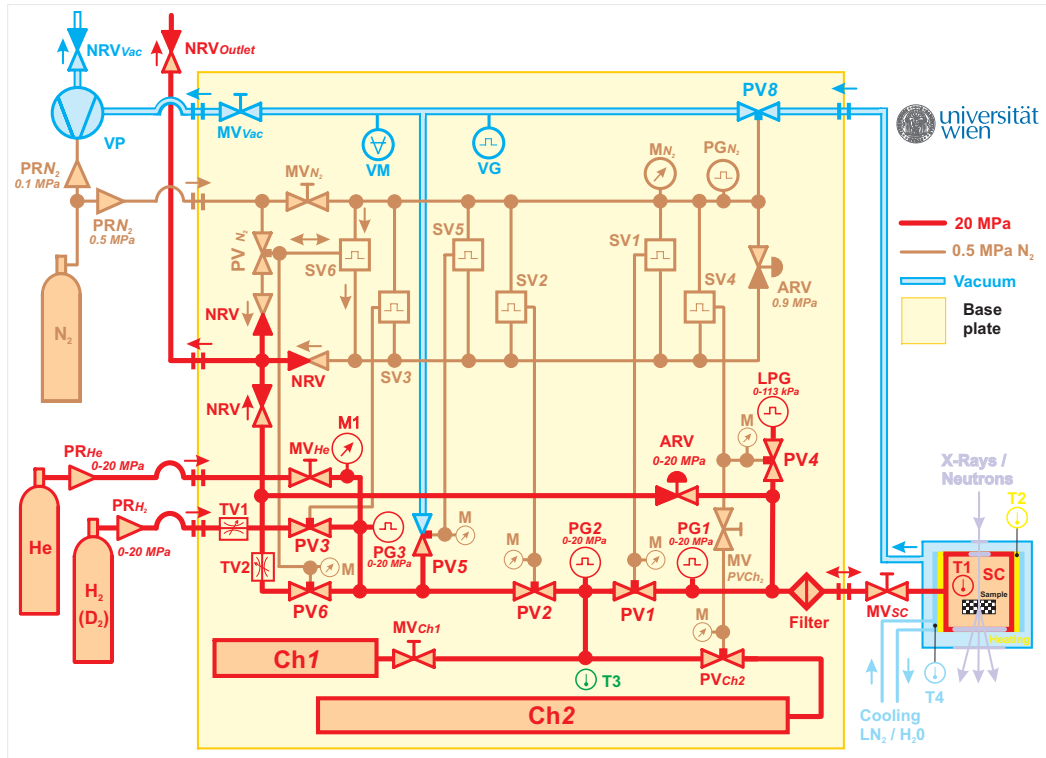
## 2.6 Hydrogenation using the Sieverts apparatus

Loading with H was performed in a portable Sieverts’ apparatus designed at the University of Vienna, see [61, 62]. Figs. 22 and 23 show a diagram and a photograph of the apparatus, respectively. The central component is an exchangeable sample chamber (SC) placed inside an evacuated security chamber. Different sample chambers can be connected for use with additional techniques (e. g. for X-ray or neutron experiments). They can be heated or cooled in a temperature range from 77 K to 820 K and operated in a pressure range from vacuum to 20 MPa (200 bar). Gaskets are all-metal made of Ni or Cu. Two reservoir chambers (Ch1 and Ch2) of calibrated volume allow to determine the amount of absorbed or desorbed gas by the volumetric method. The pneumatic valves (PV) are operated by pressure via steering valves (SV) to avoid any contact of H<sub>2</sub> with electric components. An adjustable relief valve ensures that the pressure in the system does not exceed a set value. H<sub>2</sub> is diluted with N<sub>2</sub> upon blow off via the non-return valve (NRV) which further assures that no air and oxygen enters the apparatus during this procedure. Pressurized He is used to check the apparatus for possible leaks before operation. All components except the sample chamber in its security chamber and the gas supply are fixed on a plate.

Calculating H-concentration by the volumetric method starts from the ideal gas law

$$n = \frac{pV}{RT} \quad (26)$$

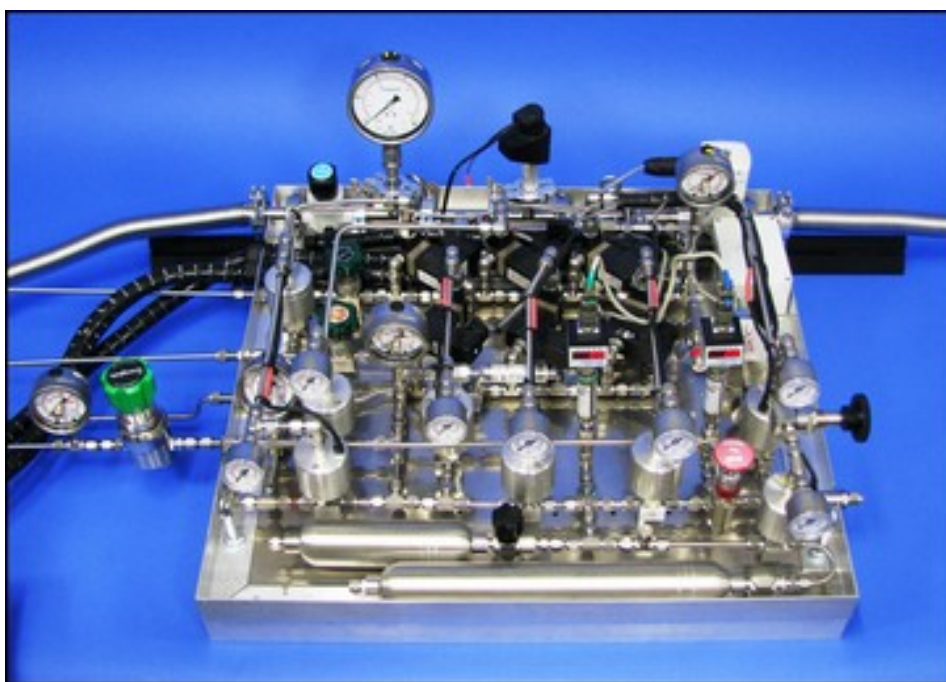
which holds for most cases met upon charging metals with H.  $n$  is the amount of gas present in the volume  $V$  at pressure  $p$  and temperature  $T$ . The amount of absorbed H can be calculated from the difference in pressure at start and end of loading. This method requires to know the exact volumes of sample and reservoir chambers.



SC .... sample chamber  
 Ch .... reservoir  
           (reference) chambers  
 M ..... manometer  
 VM ... vacuum manometer  
 PG .... (high) pressure gauge  
 LPG... low pressure gauge  
 VG.... vacuum gauge  
 T ..... thermocouple (K-type)

MV ... manual valve  
 PV .... pneumatically controlled  
           on-off valve  
 SV .... solenoid steering valve  
 ARV... adjustable relief valve  
 NRV... non-return valve  
 PR .... pressure reducer  
 VP .... vacuum pump

**Figure 22.** Schematic diagram of the Sieverts-type apparatus at the Faculty of Physics, University of Vienna

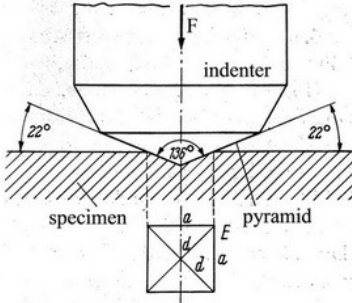
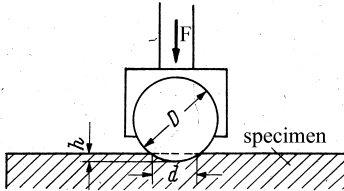


**Figure 23.** The Sieverts apparatus (without sample chamber)

## 2.7 The microhardness test

A widely established method to measure hardness of a microstructure or one of its single components is the microhardness test (MHT). With a simple set-up it facilitates to obtain results in a short time and it is applicable to a large number of materials. Several types of MHTs have been developed, the most frequently used being the Vickers test; others are Brinell, Rockwell and Knoop. All of them are based on the same principle: An object having a well-defined shape (indenter) is pressed onto a polished section of the specimen's prepared surface. The left mark's dimensions are measured after removing the indenter. For Vickers, Brinell and Knoop tests strength is calculated by forming the quotient of applied force and area of the left mark; in case of Rockwell test the depth of the left mark is used.

**Table 5.** Indenter geometries and hardness formulas for Vickers and Brinell test [63]

Vickers	Brinell
	
$HV = \frac{2F[\text{kg}] \cdot \sin 136/2}{d^2[\text{mm}^2]}$	$HB = \frac{2F[\text{kg}]}{\pi D (D - \sqrt{D^2 - d^2})[\text{mm}]}$

For Vickers and Knoop indenters are 4-sided diamond pyramids, for Rockwell and Brinell test a rounded diamond cone and a hardened steel or tungsten carbide ball is used, respectively. Indenter geometries and hardness formulas for Vickers and Brinell test appear in Table 5. Hardness values are noted in  $\text{kg mm}^{-2}$ , yet results may also be given in SI-units of pressure, i. e. Pa. Forces applied and holding times usually range on the order of 1 N and 1–10 s, respectively. In this work the formula

$$HV [\text{Pa}] = 1.8544 \frac{F[\text{N}]}{d^2[\text{m}^2]} \quad (27)$$

was used for evaluation.

## **2.8 Scanning electron microscopy (SEM)**

Scanning Electron Microscopy (SEM) uses electrons as scanning probes to image and analyze the specimen surface or near-surface area, see Fig. 24. An electron gun, commonly a tungsten cathode, releases electrons which are accelerated in a high gradient electric field to energies of 2–40 keV. Collimators concentrate these primary electrons into a beam (typical diameter 2–10 nm) incident onto the sample where they interact with shell and core electron of atoms located at the sample's surface or closely below it. The primary electrons can reach penetration depths of up to few micrometers, prompting different types of signals on their path through the sample which are collected by detectors. These signals include Secondary Electrons (SE), BackScattered Electrons (BSE), element-characteristic X-rays, sample current and cathodoluminescence. The electron beam is scanned with deflection coils along a grid over the sample as the signal for each grid point is recorded.

The most frequently used signal in SEM is the one produced by SEs (10–50 eV). They are emitted out of low sample depth hence the resolution limit is practically given by the beam's diameter. Contrast variation chiefly depends on the angle between the incident electron beam and sample surface. Since the influence of atomic number on the yield of SEs is very small, SE images are ideal for studies of surface topography.

BSE images exhibit both topographical as well as elemental contrast because of an increasing BSE yield for higher atomic numbers. These images are suited for contrasting areas of different chemical composition which can be mapped to chemical elements by Energy-Dispersive (EDS) or Wave-length Dispersive X-ray Spectroscopy (WDS).

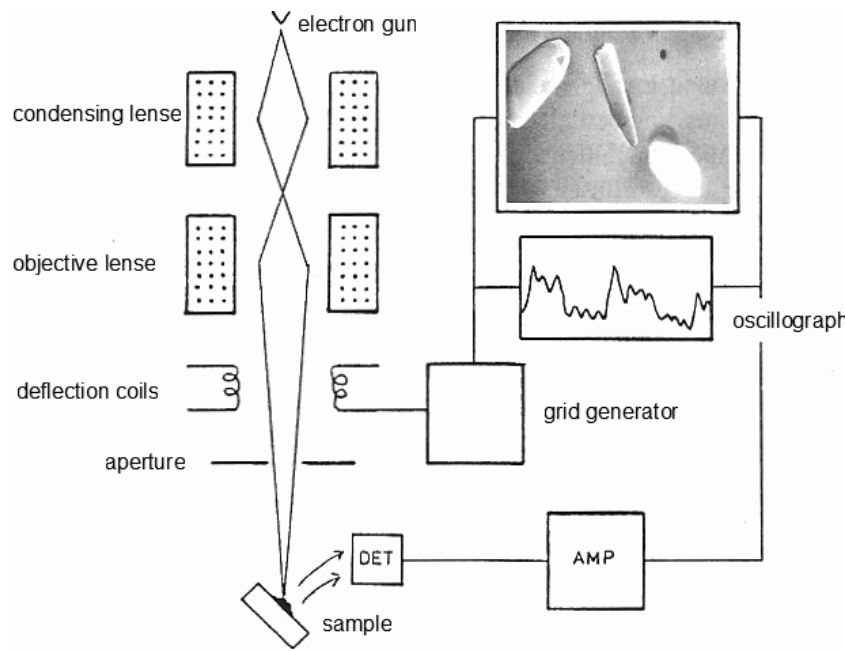


**Figure 24.** Basic components of a scanning electron microscope [64]

## 2.9 Thermal analysis

### 2.9.1 Differential scanning calorimetry (DSC)

Various processes in solids proceed only above a specific temperature limit, that is these processes are thermally activated. Examples herefore are the migration of any type of lattice defect, phase transitions or desorption processes. Differential Scanning Calorimetry (DSC) allows to identify thermal effects together with their activation energy and to determine total energies released or absorbed by the processes. For the DSC measurement the specimen and a reference material are placed in thermally isolated microfurnaces [65]. Both specimen and reference are subjected to heating over a wide temperature range at constant heating rate and the heat released or absorbed by the specimen relative to the reference is measured. Figure 25 provides an example of a DSC-scan. It is common to define heat flow into the specimen as positive, hence positive peaks correlate to endothermal processes, like a melting process or desorption of H, and negative peaks to exothermal processes, like annealing of defects. Different types of defects anneal out at different temperatures, hence identification of the peaks

observed is possible, however DSC usually needs to be combined with other methods such as XRD or electron microscopy. The total peak area gives the enthalpy released or absorbed during the process. Often the empty reference microfurnace or a second run on the specimen itself serves as reference. Normally the measurements are conducted in inert gas atmosphere to avoid specimen oxidization. Material properties accessible by DSC are e. g. heat capacity, purity, transition kinetics and migration enthalpy. The migration temperature of a lattice defect is determined by the corresponding migration enthalpy and is shifted to higher temperatures for larger heating rates applied. H. E. Kissinger [66] derived an equation which allows to extract the activation enthalpy  $e_m$  by recording annealing peak maximum temperature  $T_p$  for different heating rates  $\Phi$ .

$$\ln \frac{\Phi}{T_p^2} = -\frac{e_m}{RT_p} + \text{const.} \quad (28)$$

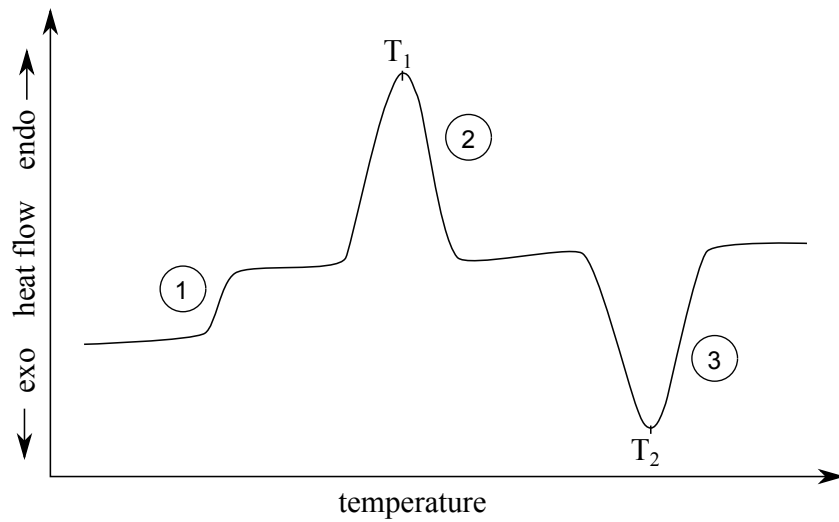


**Figure 25.** A typical DSC graph exhibiting the following features: (1) glass transition (2) endothermic peak (3) exothermic peak

### 2.9.2 Thermogravimetical analysis (TGA)

A different type of thermal testing is the ThermoGravimetrical Analysis (TGA). While at DSC, variations in heat are measured, the TGA records changes in weight during heating of a specimen at a constant heating rate. This method allows the detection of decomposition

reactions, absorption and desorption processes and specimen oxidization. Coupling TGA to mass spectrometry enables to analyze gases set free during decomposition processes.

## 2.10 Archimedean measurements

In the 3<sup>rd</sup> century B.C. Archimedes noticed that a body immersed in a liquid experiences a reduction in its apparent weight  $F$  which is proportional to the volume  $V$  of liquid displaced by the body (Archimedean principle). The Archimedean principle is not restricted to liquids and holds for gases, too. The change in apparent weight is caused by a buoyancy force counteracting the weight force on the body. The buoyancy force is equal to the weight force on the displaced volume of medium. The apparent weight is then

$$F = (\rho_S - \rho_M) \cdot V \cdot g \quad (29)$$

where  $\rho_S$  and  $\rho_M$  denote the sample's density and the medium's density, respectively. By measuring apparent mass for various medium densities the sample density can be extracted as the point of intersection of a straight line fit according to

$$m_S = -V\rho_M + V\rho_S \quad (30)$$

with the straight line  $m_S = 0$ .

## 3 Results and discussion

### 3.1 Material and initial sample preparation

The materials used in this work were Pd of purity 99.95 at% and Ti of purity 99.99 at% (both obtained from Alfa Aesar – certificates of analysis in section 5.1) machined into rods of 6.35 mm (0.25 in) diameter. Both rods were trimmed to 6.05 mm in order to match HPT-anvil cavity size. Disk shaped samples of 0.8 mm thickness were cut by spark-erosion (Charmilles Isopulse Type P25) followed by cleaning with acetone and ethanol. Before hydrogenation samples were sandblasted to ensure grip between samples and anvils later during HPT.

Table 6 on p. 45 summarizes the preparation of Pd samples regarding degree of hydrogenation and conditions of deformation by HPT.

### 3.2 Hydrogenation of Pd and Ti

#### 3.2.1 Hydrogenation of Pd

In Fig. 26 the Pressure-Concentration-Temperature (PCT) diagram for Pd appears with the loading route drawn into it. The loading proceeded along the isotherm at 300 °C to a H content of  $x \sim 0.6$  and further along the isobar at 100 bar. An isotherm above the two-phase region was chosen in order to avoid the miscibility gap and the formation of inhomogeneous internal stresses due to the misfit of lattice parameters of  $\alpha$  and  $\beta$ -phase and hence possible cracking. The procedure started with heating to 300 °C followed by isothermally increasing H<sub>2</sub>-pressure to 100 bar in steps of 10 bar to avoid strong H gradients leading to internal stresses. No activation of the Pd was necessary; already upon the first H<sub>2</sub>-pressure increase sample chamber temperature rose and H<sub>2</sub>-pressure fell again, giving evidence for the exothermic absorption reaction of H into the Pd lattice. Each pressure increase was followed by a waiting time of several hours to allow the system to attain thermodynamic equilibrium. Afterwards the sample chamber temperature was regulated down from 300 °C to RT in steps of 10 °C at constant

**Table 6.** Total H-loading ratio and HPT parameters of Pd-samples used in this work

	#10	#11	#13	#20	#28	#29	K	L	Q	R
Hydrogenation $x = 0.78$	×	×	×	×	×	×				
Hydrogenation $x = 0.73$								×	×	
77 K					×					
HPT 8 GPa 6 rot 0.2 rpm				×		×				
195 K										
220 – 265 K							×	×		
HPT 8 GPa 30 rot 0.2 rpm										

H<sub>2</sub>-pressure of 100 bar to shift the H equilibrium content further to higher concentrations. The system remained in this state for five days. To remove the samples H<sub>2</sub> gas remaining inside the sample chamber was released. The sample chamber was then opened and samples were immediately stored in LN<sub>2</sub> to prevent diffusion which would lead to loss of H.

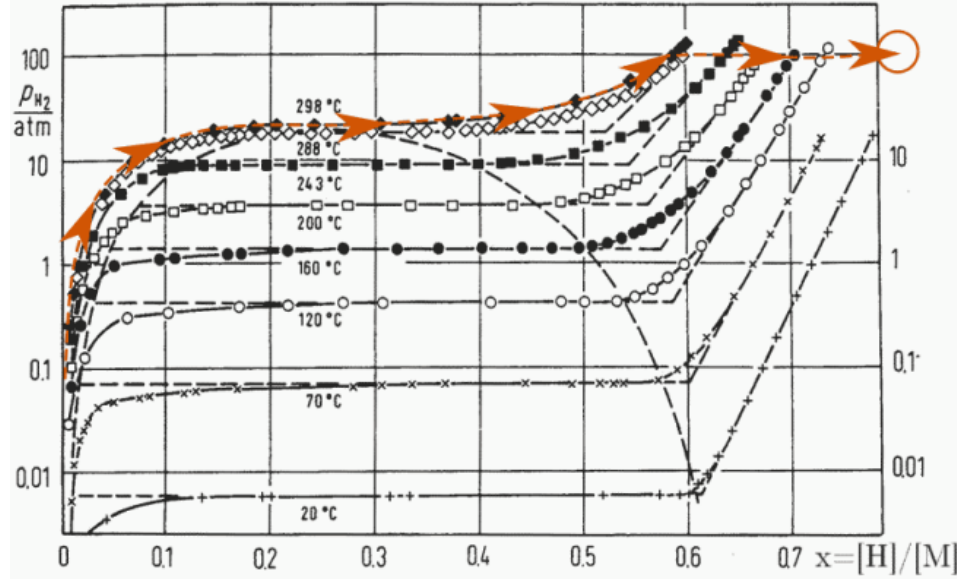


**Figure 26.** The PCT-diagram for PdH, taken from [20]. The loading route (inscribed with dashes and arrows) proceeds basically along the isotherm at 300°C above the two-phase region in order to avoid the internal stresses caused by the lattice misfit between the low-concentration  $\alpha$  and the high-concentration  $\beta$ -phase.

The final H-concentration was determined for three samples by weighing under air right before transferring into LN<sub>2</sub>. A H to Pd atomic ratio of at least 0.78 was reached, see Table 7

**Table 7.** Pd sample masses before and after loading with H. Weighing was performed on a Sartorius M3P microbalance.

	unit	Pd#10	Pd#11	Pd#20
m(Pd)	mg	225.16	558.79	272.06
m(PdH)	mg	226.84	562.95	274.10
m(H)	mg	1.68	4.16	2.04
$c_H$	at%	44.1	44.0	44.2
$x$	[H]/[Pd]	0.78	0.78	0.79

on p. 46. Figures 27 and 28 on p. 48 show images of Pd taken with the optical microscope before and after loading with H. The former flat surface is broken into facettes of different orientation. These images demonstrate the macroscopical structural change taking place upon hydrogenation.

### 3.2.2 Hydrogenation of Ti

Three samples of Ti (99.99 at%) were loaded with H. In order to be able to use the more sensitive low pressure gauge (LPG in Fig. 22 on p. 37) a H<sub>2</sub>-pressure below 1.3 bar (upper limit of LPG) was chosen. Both reservoir chambers Ch1 and Ch2 were filled with H up to a pressure of 1.1 bar. At RT no absorption of H by Ti could be observed within a period of five days. Upon heating the sample chamber to 450 °C H<sub>2</sub> started to get absorbed and H<sub>2</sub>-pressure dropped to a constant value of 0.6 bar within 18 h. From the changes in H<sub>2</sub>-pressure a H-concentration of  $x = 1.93$  was calculated (volumetric method), in excellent accordance with the gravimetric method (Table 8 on p. 47) and equilibrium H-concentration read from the PCT-diagram for TiH (Fig. 29 on p. 49).

**Table 8.** Ti sample masses before and after loading with H. Weighing was performed on a Sartorius M3P microbalance.

	unit	Ti#51	Ti#52
m(Ti)	mg	97.583	100.65
m(TiH)	mg	101.52	104.69
m(H)	mg	3.94	4.04
$c_H$	at%	65.7	65.6
$x$	[H]/[Pd]	1.92	1.91

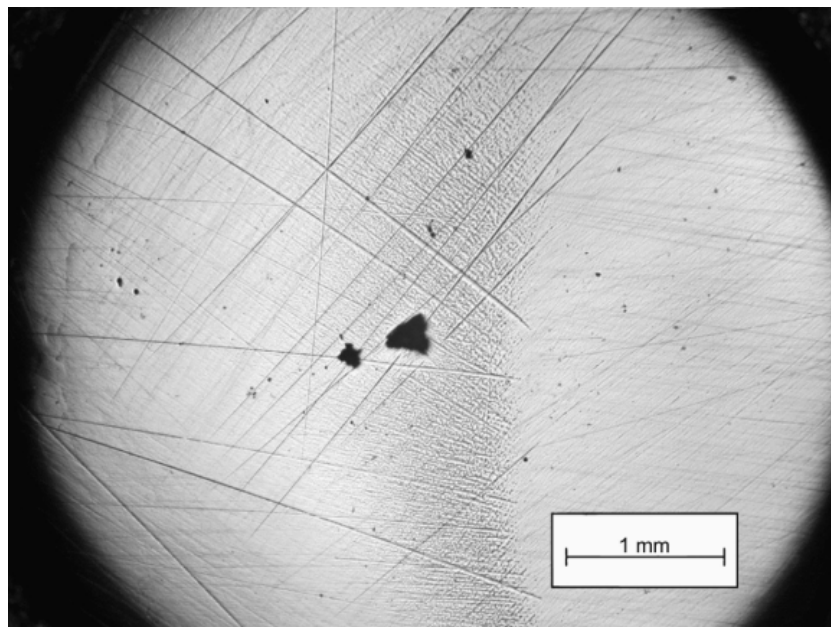


**Figure 27.** Surface of mechanically polished as-received Pd

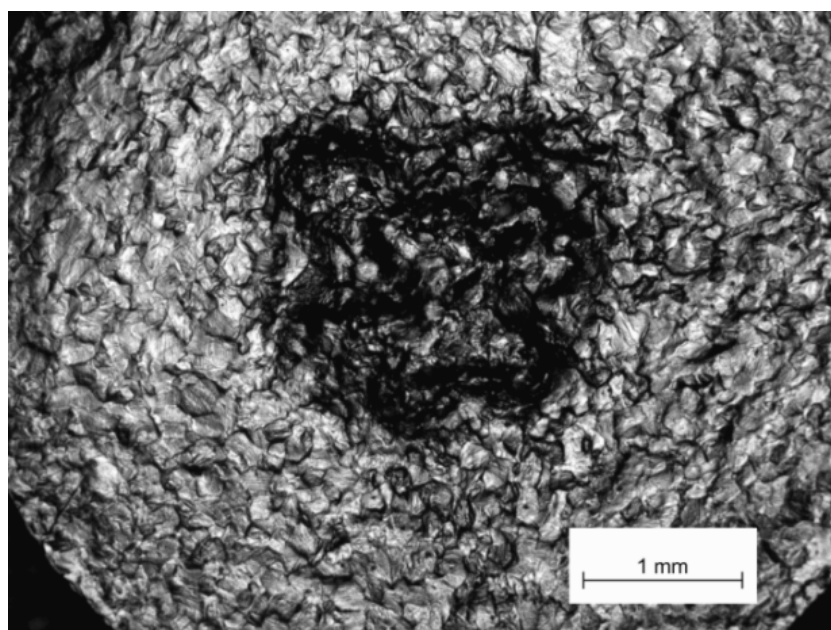


**Figure 28.** Pd sample from Fig. 27 after loading with H. The lattice expansion due to H uptake of differently oriented grains causes roughening of the surface. Upon hydrogenation the material can be macroscopically deformed, as can be seen from the depression at the center of the sample surface, appearing as a dark region.

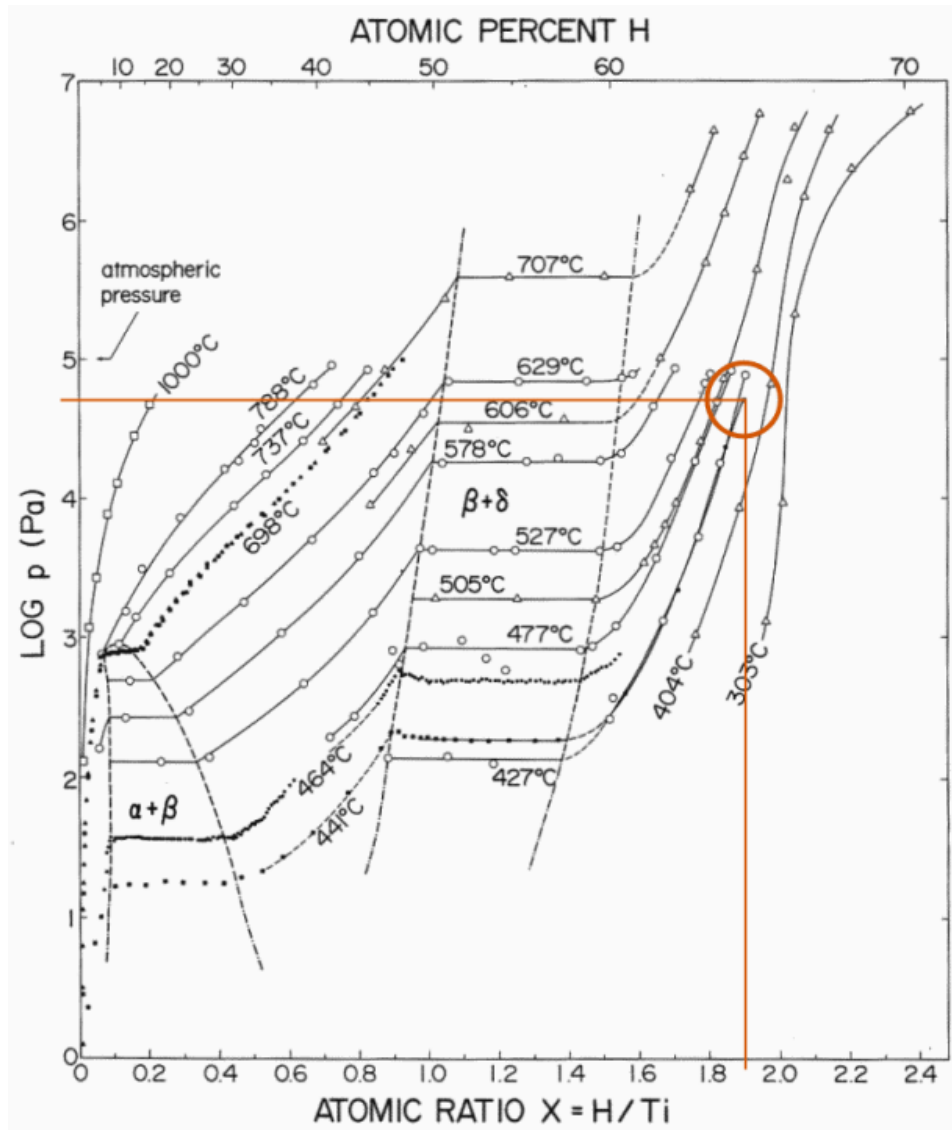


**Figure 29.** The PCT-diagram for TiH, taken from [27]. The state of equilibrium attained is marked with an open circle and corresponds to a H-concentration of  $x \sim 1.93$  at a H-pressure of 0.6 bar =  $6 \cdot 10^4$  Pa.

### 3.3 Desorption measurements

To characterize desorption of H from Pd at RT in air two samples of  $\text{PdH}_{0.78}$  were placed on a balance (Sartorius M3P, display accuracy  $1\text{ }\mu\text{m}$ ) and the evolution of mass recorded over time. Initial warming of samples from 77 K to RT was done in Ar atmosphere in order to avoid condensation of water. Measurements were recorded every 10 s. The process was controlled via PC by a script written for that purpose, see 5.1. Figures 30 and 32 show the resulting plots (masses in the unloaded state determined before hydrogenation were 558.790 mg and 287.817 mg, respectively).

The desorption proceeds faster in the sample with lower mass. In this sample 3/4 of the H is released within 27 h and after 110 h no significant change in mass is observed any more. On the other hand the sample with higher mass retains at least 3/4 of the initial H content after 27 h. Even after  $25 \cdot 10^5\text{ s}$  (28 d) H is still present in the sample and desorbing and hence sample mass is decreasing. Converting the plot in Fig. 30 into a double logarithmic scale shows three straight-lined segments, see Fig. 31. Each segment can be represented by a functional relation according to

$$y = ax^b. \quad (31)$$

Corresponding graphs are drawn into Fig. 30 and 31. The nature of the kinks is unclear, yet a few things can be said. The kinks did not occur for the low mass sample, see Fig. 33. The second kink, which is well visible in Fig. 31 appears at a H-concentration of  $x \sim 0.6$ , which corresponds to the terminal solubility limit of H in Pd at RT (see Figs. 16 on p. 27 and 26 on p. 46), and therefore might be related to the transition from the  $\beta$ -phase to the two-phase region.

Two major experimental difficulties were encountered when performing the measurements:

1. Balance drift: Under load of a test object of constant mass the displayed mass drifts to lower values, as shown in Fig. 34 on p. 53. This effect might account for masses undershooting initial masses of non-loaded pure Pd samples during desorption (Figs. 30 and 32). This behaviour is of pure technical nature, and is evoked under permanent

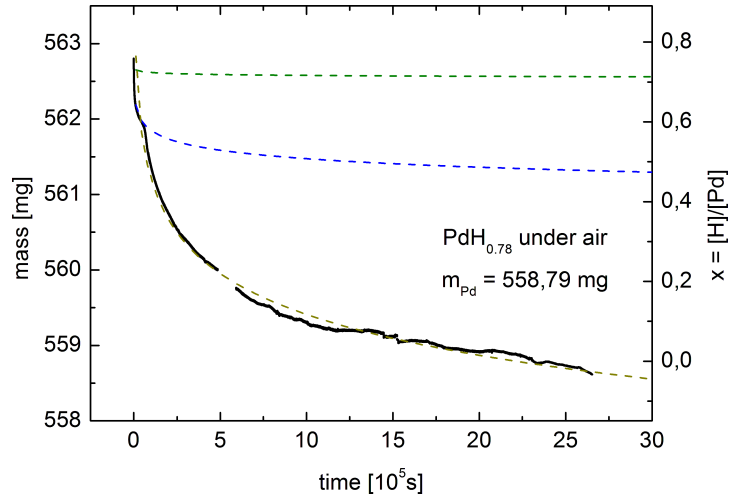


**Figure 30.** Evolution of mass of sample Pd#11 (high mass) as H desorbs under ambient conditions in air

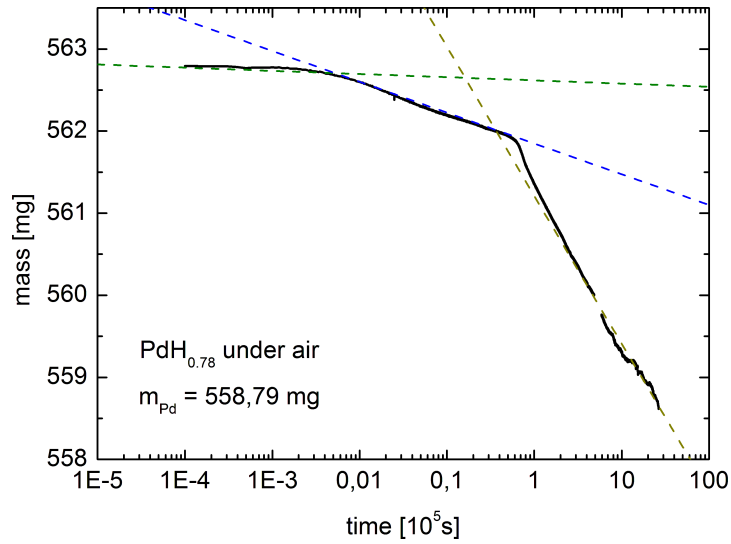


**Figure 31.** The logarithmic version of Fig. 30 clearly demonstrates three segments of power-law like behaviour for the mass of sample Pd#11 (high mass) during desorption of H.

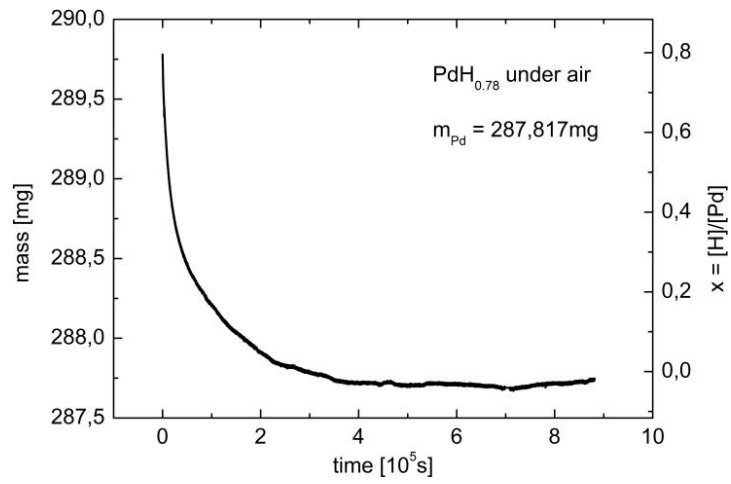


**Figure 32.** Evolution of mass of sample Pd#13 (low mass) as H desorbs under ambient conditions in air

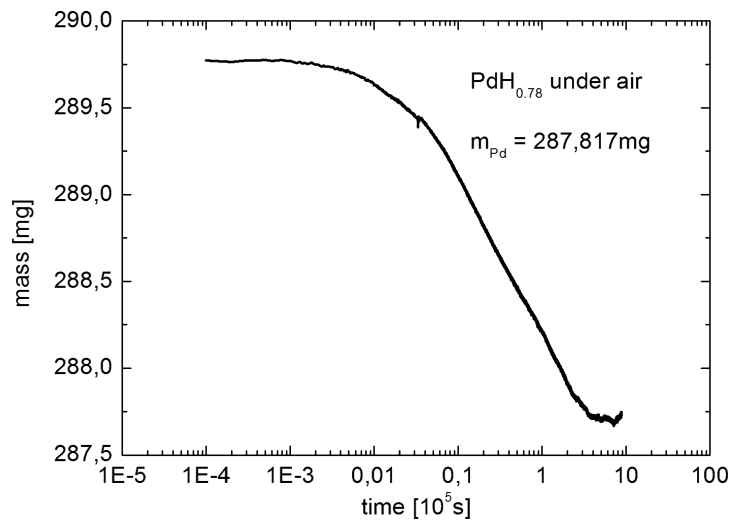


**Figure 33.** The logarithmic version of Fig. 32

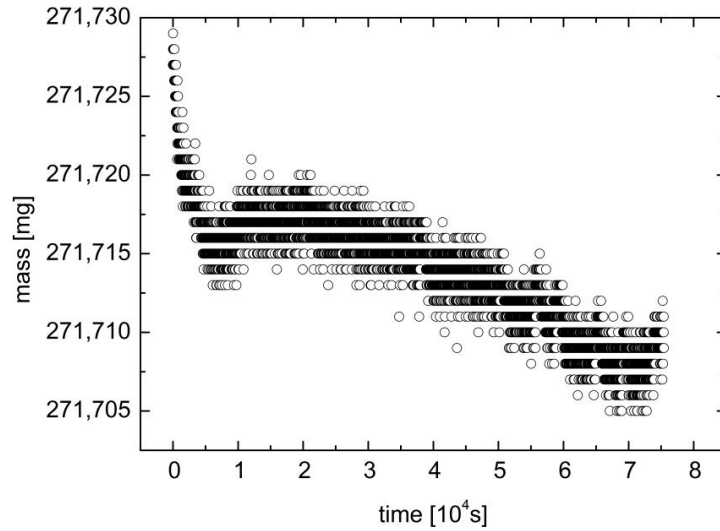


**Figure 34.** Balance drift (Sartorius M3P) under load at constant mass within  $\sim 21$  h. The vertical structuring into horizontal bands arises from the display accuracy of  $1 \mu\text{g}$ .

loading by a warming of the weight compensation electronics.

2. Unstable environment: The measurement is very sensitive to changes in environmental parameters, e. g. air flow and temperature. Data points had to be removed due to large deviations caused by air flow (see gap at  $5 \cdot 10^5$  s in Fig. 30).

### 3.4 Microhardness tests

The aim of these studies was to record microhardness in the course of desorption of interstitial H from Pd at RT. therefore sample Pd#10 was first mechanically polished on one circular area, then loaded with H up to a concentration of  $x = 0.78$  and afterwards stored at RT. The tests were conducted with a AP PAAR MHT-4 testing device mounted on an optical microscope (Zeiss Axioplan). Every test series consisted of ten marks each applied by a load of  $0.5 \text{ N}$ ,  $10 \text{ s}$  holding time and a load gradient of  $1 \text{ N s}^{-1}$ . The sample was always placed loosely on the holder. For each test series sample mass was measured (Sartorius M3P) to determine the corresponding H concentration. For the as-received Pd a hardness of  $(1.4 \pm 0.1) \text{ GPa}$  was obtained.

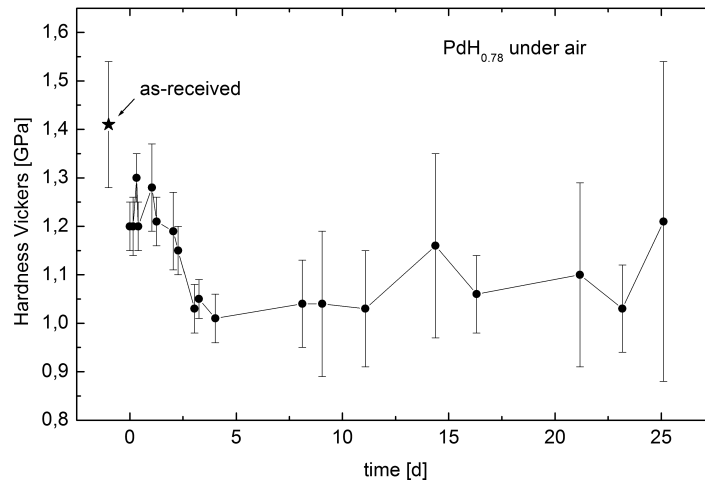


**Figure 35.** Evolution of Vickers hardness with time for  $\text{PdH}_{0.78}$  stored at RT. The error bars represent standard deviation of the corresponding series of 10 marks.

Figure 35 shows the temporal change of microhardness after hydriding. The initial hardness of PdH is smaller by 0.2 GPa compared to the as-received Pd, which can be explained by recovery processes and relaxation of internal stresses during heating to 300 °C upon hydriding. Two days after the start of desorption microhardness drops from 1.2 GPa to 1 GPa in the course of which the scatter remains roughly constant but from the fifth day on the scatter increases with time. It has to be pointed out that the error bars (standard deviation of 10 marks for each point) shown in Figs. 35 and 36 represent *real scattering* of microhardness across the sample and are not of experimental nature, like e. g. an instrumental error would be.

These features might be explained by comparison with Fig. 36, where microhardness is plotted against the fraction of H still present in the sample, combined with the phase diagram for PdH (Fig. 16). It can be seen that the drop in hardness correlates with the transition from the single-phase  $\beta$  region into the two-phase region. At the same time the appearance of bright stripes is observed, which are interpreted to be the newly forming  $\alpha$ -phase, see Fig. 37.

The increase in statistical scatter of hardness with time can be understood as follows: Due to the increase in fraction of the softer solid solution  $\alpha$ -phase the indenter presses either upon the pure  $\beta$  or  $\alpha$ -phase or a mixture of both resulting in higher, lower or hardness values inbetween.

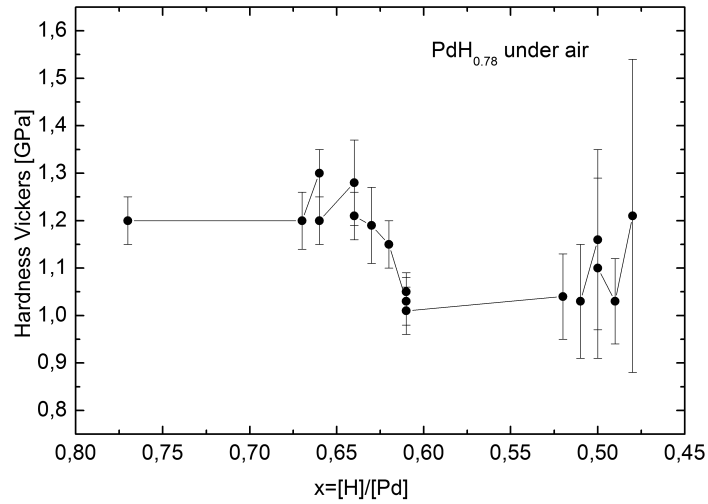


**Figure 36.** Vickers hardness of  $\text{PdH}_{0.78}$  plotted against H concentration during desorption. The drop in microhardness from 1.2 GPa to 1 GPa at  $x \sim 0.65$  corresponds to the transition from the single-phase  $\alpha$ -region into the miscibility gap, confer Fig. 26 on p. 46.

Hence a Vickers hardness of  $\sim 1.2$  GPa and 1 GPa was attributed to the  $\beta$ -phase and  $\beta + \alpha$  mixture, respectively. Hence the  $\alpha$ -phase needs to exhibit a hardness below 1 GPa.

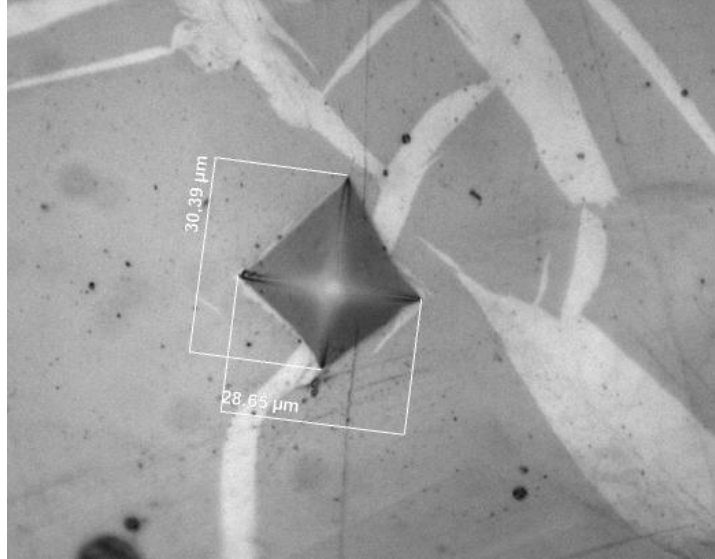


**Figure 37.** Below a concentration of  $x \sim 0.65$  the material is a mixture of the high-concentration  $\beta$  and the low-concentration  $\alpha$ -phase, the latter appearing brighter under the optical microscope. The central dark four-sided figure is the left mark of the indenter. It presses either onto a single-phase region or onto a mixture of both phases, as seen above.

### 3.5 Deformation by HPT

All deformations were performed with the HPT equipment at ESI Leoben, Austria [67]. All samples had an identical diameter of 6 mm and identical thickness of 0.8 mm before HPT. All samples were processed at a pressure of 8 GPa and rotation speed of 0.2 rpm independent of deformation temperature. Equivalent strains were calculated using definitions 15 and 16. Thickness of samples was reduced to  $\sim 0.6$  mm by HPT. For deformations below RT a specially designed bowl, which encloses the lower anvil and can be filled with a cooling agent, was utilized, see Fig. 38.

#### 3.5.1 Deformation under $\text{LN}_2$

Seven samples of  $\text{PdH}_{0.78}$  were deformed at the temperature of 77 K, which was attained by cooling the anvils with  $\text{LN}_2$ . The deformation temperature was chosen for two reasons, namely (i) in order to avoid loss of H during deformation and (ii) to examine the effect of



**Figure 38.** The anvil region of the HPT-facility at ESI Leoben, Austria, during operation at temperature of frozen CO<sub>2</sub> (195 K).

deformation temperature on the exothermic peak in DSC measurements found at 482 K and ascribed to the annealing of Vac-H clusters, as well as on the the peak attributed to recovery and recrystallization processes [16]. Five samples were deformed to a total of 6 rotations ( $\varepsilon = 73$ ), one each to 1 ( $\varepsilon = 12$ ) and 0.5 rotations ( $\varepsilon = 6$ ). Before placing the samples into the HPT device, the anvils were sandblasted and pre-cooled for 30 min in the mounted state. Afterwards the sample was transferred directly from LN<sub>2</sub> into the anvil cavity and deformed. In Fig. 39 the torque graphs for the five samples deformed to 6 rotations are shown, which serve as a well-suited tool to detect anvil slip. If anvil slip occurs the torque is substantially reduced, which results in a lower torque build-up or a drop to a lower level, see Fig. 40 on p. 58 for the former case. To avoid anvil slip the cavities were sandblasted after every second run, except for low-grade deformations. A heater blower was used for defreezing the anvil region before unmounting them.

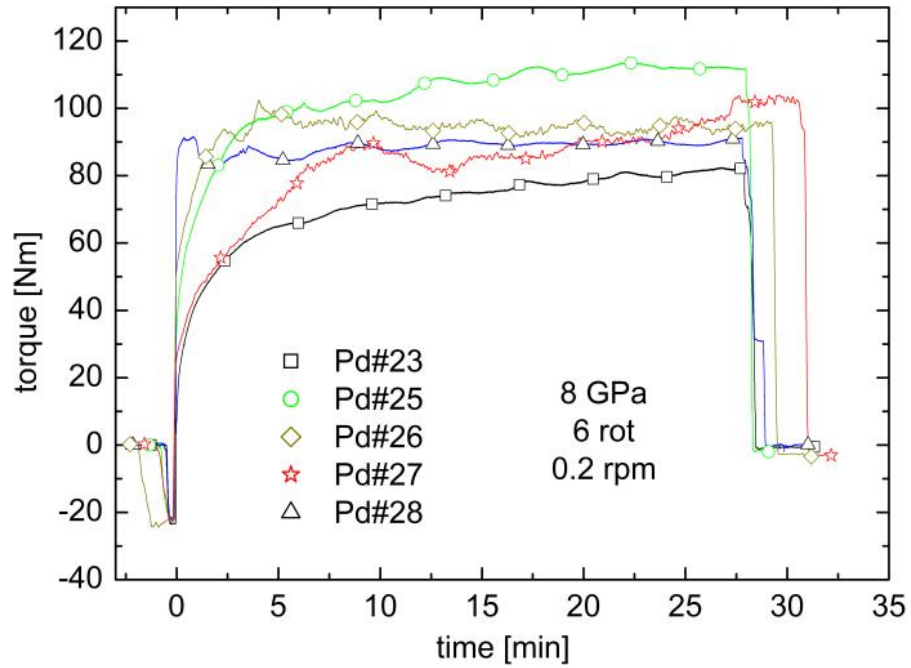


**Figure 39.** Torque graphs for 5 samples of  $\text{PdH}_{0.78}$  deformed at temperature of  $\text{LN}_2(77\text{ K})$

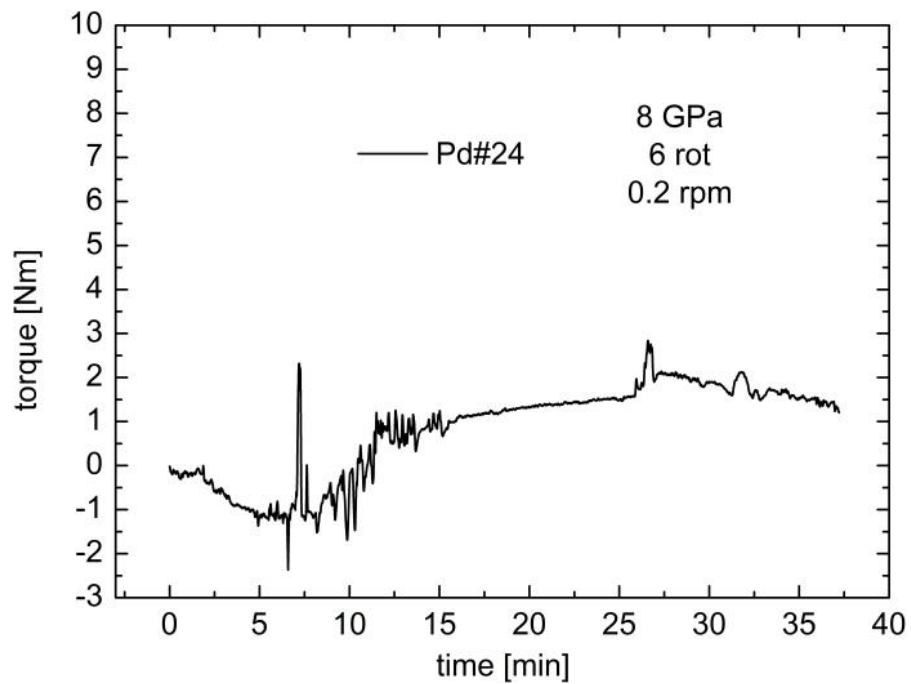


**Figure 40.** In case of anvil slip the torque build-up is substantially smaller than in the well-adhering case, compare to Fig. 39.

### 3.5.2 Deformation under CO<sub>2</sub>

Altogether three samples of PdH<sub>0.78</sub> were deformed at temperature of frozen CO<sub>2</sub> (195 K) to a total of 6 rotations ( $\varepsilon = 73$ ). This temperature was chosen because (i) the samples deformed at 77 K did not show the presence of the DSC-peak at 482 K and (ii) to establish a deformation temperature below 220–265 K, which was done in [16]. Before mounting the anvils were sandblasted and deposited in frozen CO<sub>2</sub> for 40 min for each run. After mounting the anvil region was further cooled with the anvils in the closed state. In Fig. 41 the torque graphs are shown.

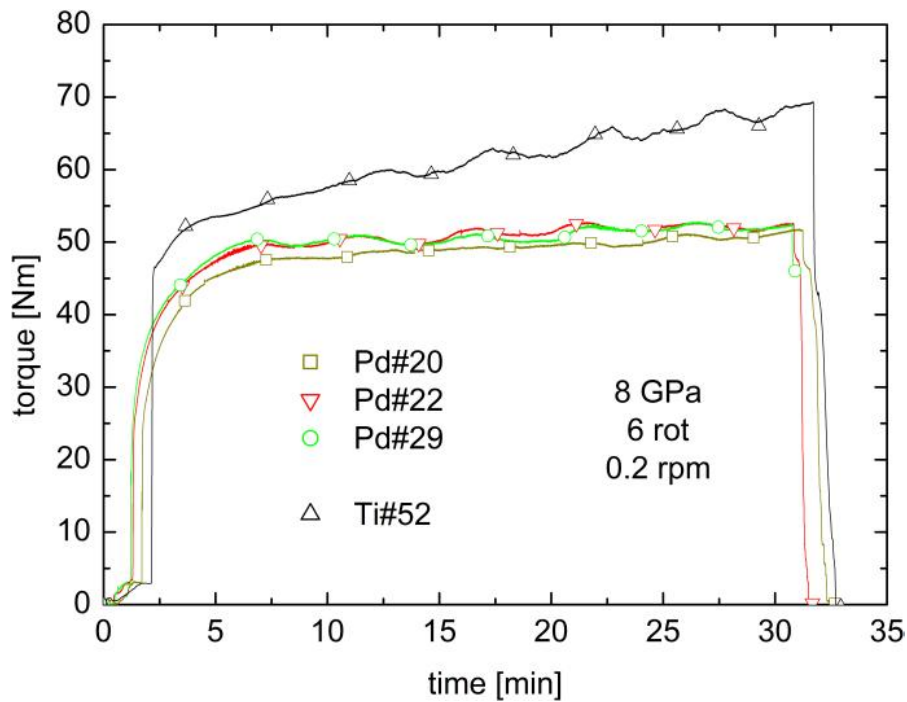


**Figure 41.** Torque graphs for three specimens of PdH<sub>0.78</sub> deformed at temperature of frozen CO<sub>2</sub> (195 K) and for TiH<sub>1.91</sub> deformed at RT

### 3.5.3 Deformation of TiH<sub>1.91</sub>

One sample of TiH<sub>1.91</sub> (fct  $\varepsilon$ -phase according to [27]) was deformed at RT to a total of 6 rotations ( $\varepsilon = 73$ ) at a pressure of 8 GPa and 0.2 rpm, see Fig. 41. This demonstrated that

HPT facilitates high-grade plastic deformation of even highly brittle materials like  $\text{TiH}_2$ .<sup>5</sup> Still the experimental procedure remains difficult due to easy cracking of the sample upon closing the anvils.

### 3.6 Differential scanning calorimetry (DSC)

In order to fit into the DSC crucibles the diameter of all samples was mechanically reduced, if necessary, below 6 mm using a pair of pliers and abrasive paper followed by cleaning in ethanol in the ultrasonic bath. Open Al crucibles were used for all DSC measurements which were performed with a Netzsch DSC 204 Phoenix (sensitivity  $0.05 \text{ J g}^{-1}$ ) operated with Ar as purge gas. The heating rate and cooling rate were  $5 \text{ K min}^{-1}$  and  $10 \text{ K min}^{-1}$ , respectively,  $\text{LN}_2$  served as cooling agent.

#### 3.6.1 DSC of Pd

Measurements on Pd were recorded in a temperature range from RT to 873 K. For all samples two heating runs were recorded the second of which was employed as the reference for the first one. After all measurements a bluish staining of the sample surface could be observed which hints at slight sample oxidization during heating.

In Fig. 42 DSC graphs of  $\text{PdH}_{0.78}$  deformed at 220–265 K to  $\varepsilon = 84$  together with  $\text{PdH}_{0.78}$  deformed at 77 K to  $\varepsilon = 73$  are presented. The former is taken from [16] and shows the presence of a prominent exothermic peak at 482 K (total peak energy  $1.17 \text{ J g}^{-1}$ ) which was interpreted to correlate with the annealing of point-type defects by making use of in-situ TEM investigations during heating. This peak was then ascribed to the decomposition of Vac-H clusters which had formed *during* the deformation by HPT. The broad exothermic peak in the higher temperature range between 535 K and 750 K was related to recovery and recrystallization processes coupled to the annealing of dislocations and grain boundaries.

---

<sup>5</sup>When an attempt was made to mechanically reduce the diameter of  $\text{TiH}_{1.91}$  by filing the sample immediately cracked, as opposed to  $\text{PdH}_{0.78}$  which could be filed.

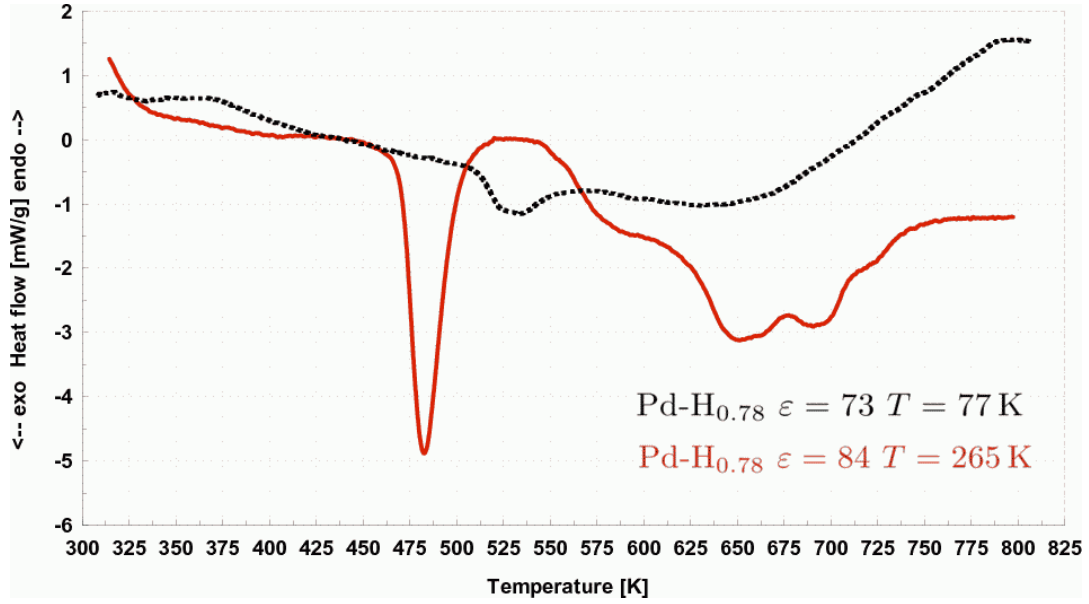


**Figure 42.** DSC graphs of hydrogenated Pd HPT-deformed at 8 GPa at temperatures of 220–265 K and 77 K. The latter sample does not show the exothermic peak at 482 K attributed to the annealing of Vac-H-clusters.

Surprisingly, the sample deformed at 77 K exhibits no sign of the exothermic peak found at 482 K in samples deformed at 220–265 K. The interesting part of this phenomenon lies in the fact that despite the high loading ratio of  $x = 0.78$  (which corresponds to about 5 of 6 of octahedral sites being occupied) Vac-H clusters did not form. The following reasons may be responsible for that observation: First, the formation of Vac-H clusters is a thermally activated process the activation temperature of which may be found in the range between 77–220 K. If so, insufficient mobility at 77 K will inhibit H atoms and vacancies in the Pd-lattice from encountering each other in time. Second, at high H concentrations a H-ordered low-temperature phase, related to the so-called 50 K anomaly, exists in Pd-H [68,69]. For a H-concentration of  $x = 0.78$  the transition temperature is  $\sim 80$  K, see Fig. 16, however, short-range order is observed even up to considerably higher temperatures. Interactions between H atoms causing the ordering might hamper H movement across interstitial lattice sites, thereby preventing segregation of H atoms to non-adjacent vacancies.

Figure 43 shows DSC graphs of PdH<sub>0.78</sub>-samples deformed at 195 K to  $\varepsilon = 73$  which were

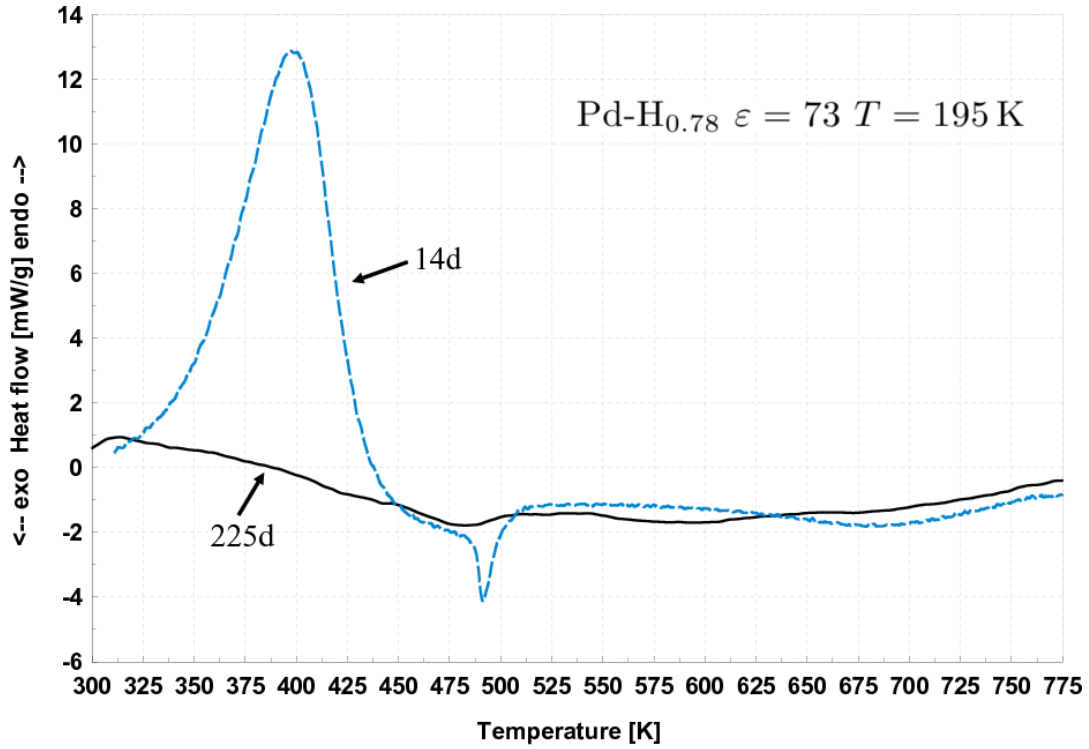


**Figure 43.** DSC graphs of hydrogenated Pd HPT-deformed at 8 GPa at 195 K recorded after different periods of storage at RT following HPT

stored at RT after HPT for a period of 14 d and 225 d, respectively. In the former case, that is for a storage time of 14 d, a large endothermic peak appears between 300 K and 450 K caused by desorption of H from interstitial sites. At 482 K an exothermic peak with total peak energy of  $0.25 \text{ J g}^{-1}$  is found and considered to relate to the decomposition of Vac-H clusters, as in Fig. 42. The fact that the peak is smaller than the one found in samples which were identically prepared except for the much shorter period of storage time at RT (14 d) might be explained as follows: Either the reduction in magnitude is caused by superposition of the right side of the H-desorption peak or less Vac-H clusters are formed during HPT at 195 K compared to HPT at 220–265 K. The latter lends support to the first part of the reasoning provided above to explain the observations presented in Fig. 42. To our surprise in samples deposited at RT for a longer period of 225 d to allow for complete desorption of interstitial H (but otherwise identically prepared) the peak at 482 K was further reduced in magnitude and simultaneously broadened or shrank below the detection limit, hence vanished. This observation suggests in

contrast to observations made by Y. Fukai on electrodeposited Cu stored for 32 a [10], that Vac-H clusters in PdH are not stable at RT but disintegrate on a time scale of several months.

### 3.6.2 DSC of Ti

Measurements were performed on a H-loaded ( $x = 1.92$ , 65.8 at%) non-HPT-deformed sample (Ti#51) in a temperature range from RT to 1000 K. The aim was to provide DSC-curves for comparison with following DSC-measurements on HPT-deformed TiH.

The first three heating and cooling cycles, presented in Fig. 44, were carried out from RT to 850 K. The first heating run exhibits an endothermic peak both at 746 K and 807 K, respectively. Further at higher temperatures the DSC signal rises strongly indicating the presence of another large endothermic peak. The former two peaks vanish after the first heating, yet a small reproducible endothermic peak appears at  $\approx 610$  K. All three cooling runs feature an exothermic peak of roughly the same size at  $\approx 500$  K. To record the endothermic peak above 850 K the temperature range maximum was extended to 950 K, see Fig. 45. Again this peak is only present in the first heating run.

The three endothermic peaks vanishing upon first heating are considered to arise from desorption of H from the Ti host lattice. The results agree very well with DSC-measurements on  $\text{TiH}_2$  presented in [70]. The onset of H desorption is at  $\approx 450^\circ\text{C}$ . The recurring peaks are considered to stem from a phase transition. The temperature difference between the peak positions in heating and in cooling curves represent a hysteresis effect. A combination of the DSC-graphs above with the temperature-composition phase diagram of TiH (Fig. 46 on p. 65) suggests that the peaks correlate either with the transition  $\alpha + \beta \text{ TiH} \rightarrow \alpha + \delta \text{ TiH}$  or the transition  $\alpha \text{ TiH} \rightarrow \alpha + \delta \text{ TiH}$  at H-concentrations below 6.72 at%.

It has to be pointed out that the paths described in Fig. 46 are only tentative and for a precise determination of their positions the DSC-measurements would need to be coupled to thermogravimetry or X-ray diffraction.

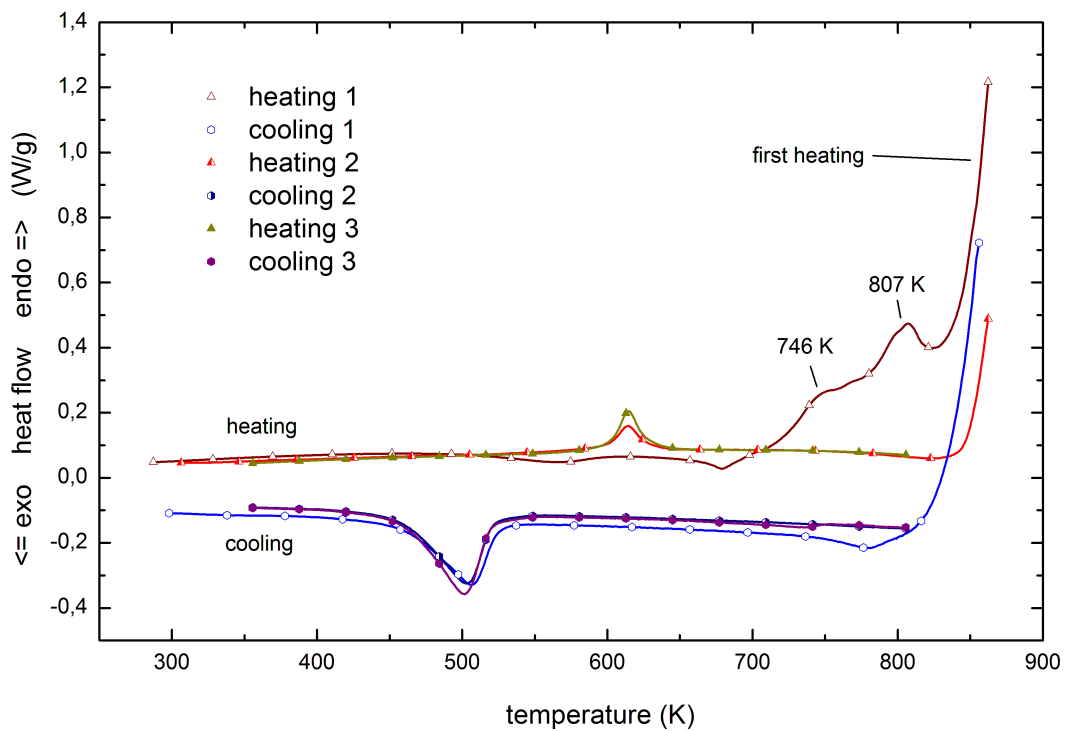


**Figure 44.** DSC graphs (RT to 870 K) of  $\text{TiH}_{1.91}$

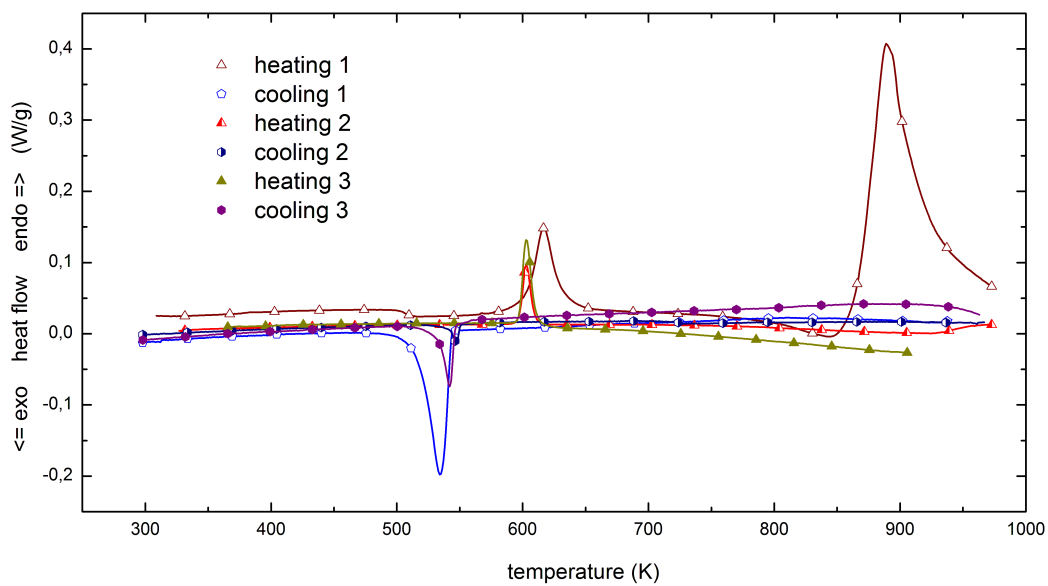


**Figure 45.** DSC graphs (RT to 950 K) of  $\text{TiH}_{1.91}$

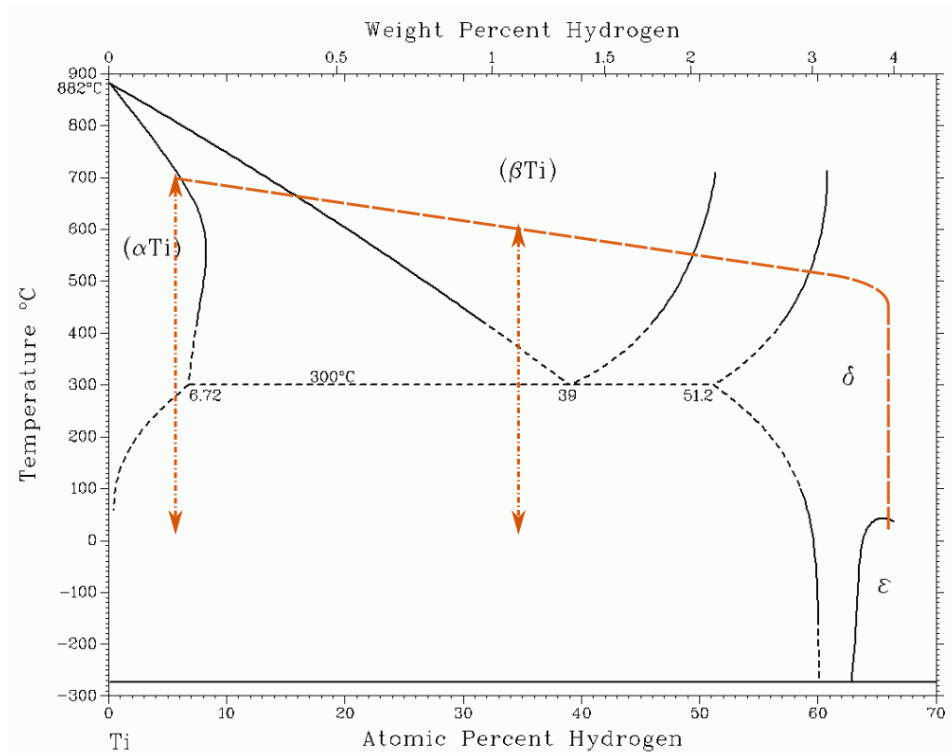


**Figure 46.** Schematic path of the evolution of  $\text{TiH}_{1.92}$  upon isochronal heating. The vertical lines (dot-dashes) represent the paths of repeated heating and cooling. After [70]

### 3.7 SEM-investigations

Samples K and L were used for investigation by Scanning Electron Microscopy (SEM). Pd L had been loaded with H up to a concentration of  $x = 0.73$  whereas Pd K remained unloaded and subsequently both samples were deformed by HPT at a temperature of 220–265 K and pressure of 8 GPa to a total of 30 (!) rotations (equivalent strain  $\varepsilon = 435$ ), see Table 6. Before investigation by SEM samples were additionally heat-treated for 1 h at 1073 K in UHV and mechanically polished (ultimate grain size 0.05  $\mu\text{m}$ ) afterwards. For polishing samples were glued onto polishing dies with commercially available glue (UHU hart). Ethanol was used for dissolving the glue and further cleaning of the samples. (Acetone proved to be unsuited due to drying blotches.)

Studies were performed in a Zeiss Supra 55VP using the SE-detector at an acceleration voltage of 20 keV. A region of 65  $\mu\text{m} \times 65 \mu\text{m}$  at the sample surface was divided into a grid of  $6 \times 6$  overlapping images, each comprising an area of 200  $\mu\text{m}^2$ . The single images overlapped each other by at least one forth of their lateral length. Finally the images were stitched into a panorama.

Inspection of Pd L revealed the existence of a large number of pores at the sample free surface, see Fig. 47. They are interpreted to be voids of vacancies that agglomerated during heat treatment, as reported in related literature [57, 71]. To deduce the volume fraction of pores the image in Fig. 47 was segmented into black and white, see Fig. 48. The grey value threshold was manually adjusted in such a way that as many pores as possible remained visible. Scratches on the sample surface then were erased by hand. The pores are not equally distributed over the sample surface but assemble into regions of lower and regions of higher pore concentration. Furthermore, in such regions of high concentration they primarily segregate to grain boundaries, thereby forming a net-like arrangement. By stereological analysis of the segmented SEM image, a value of  $2.8 \cdot 10^{-2}$  for the local concentration of vacancies was derived.<sup>6</sup>

---

<sup>6</sup>Provided the pores are stochastically distributed throughout the sample their average volume fraction equals the average area fraction in any random section (Delesse's Principle), see [72].

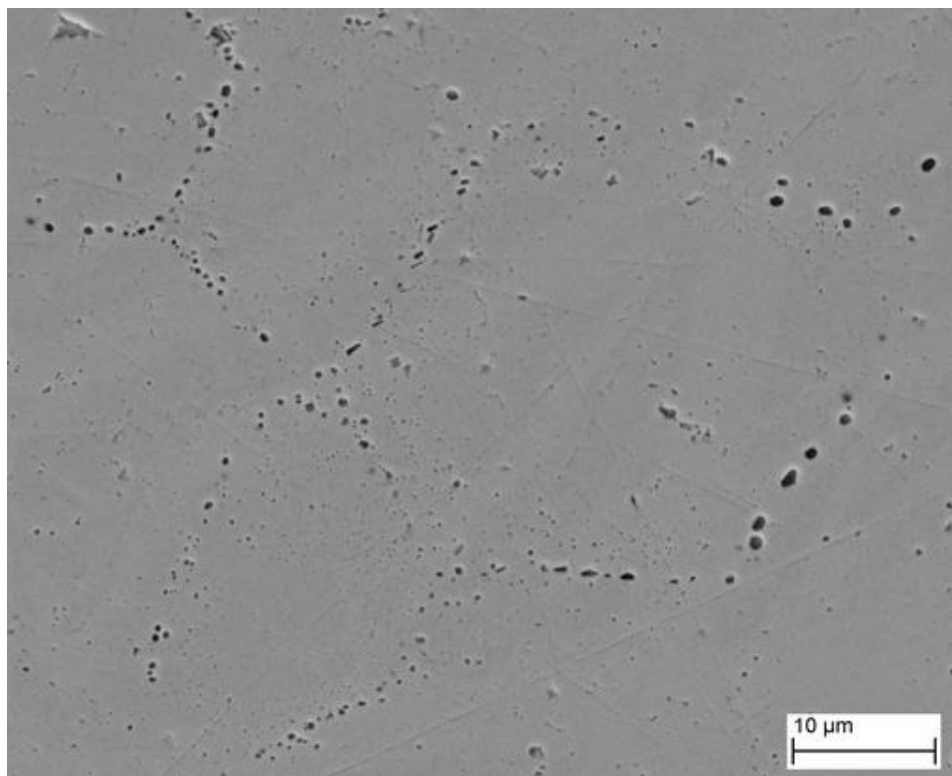


**Figure 47.** Heat treated Pd (sample L) which had been hydrogenated and subsequently HPT-deformed shows pores at the free surface. These pores are considered to have formed by agglomeration of vacancies during heat treatment for 1 h at 1073 K in high vacuum.

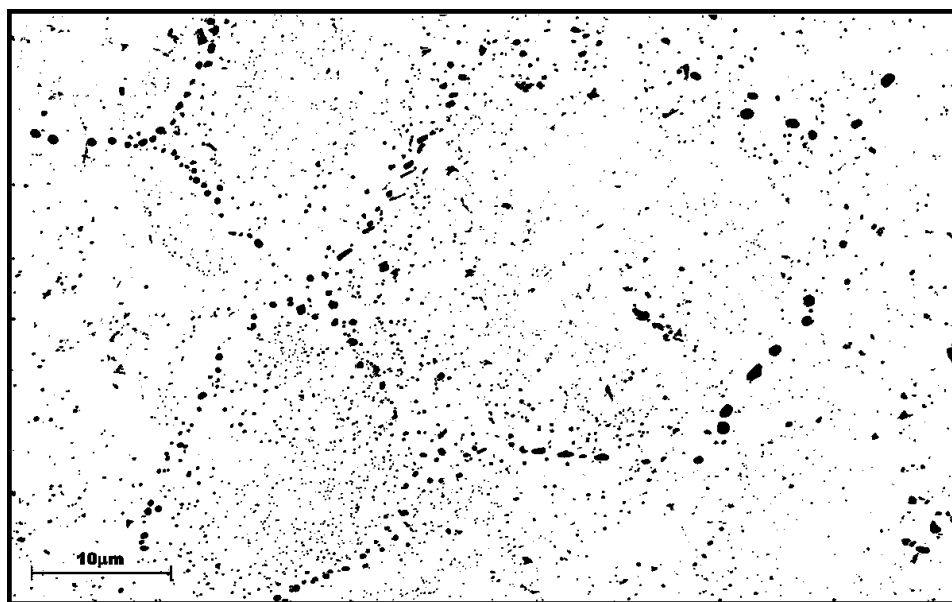


**Figure 48.** Figure 47 segmented into black and white showing the pores as black spots

In contrast a considerably smaller number of voids was found on the free surface of Pd K (pure Pd, HPT 220–265 K 30 rot), see Fig. 49. A vacancy concentration of  $3.1 \cdot 10^{-3}$ , that is one order of magnitude smaller compared to the value for hydrogenated and HPT-deformed Pd (sample Pd L), was derived. These results clearly show the favourable influence of interstitial H on the formation of vacancies in Pd.

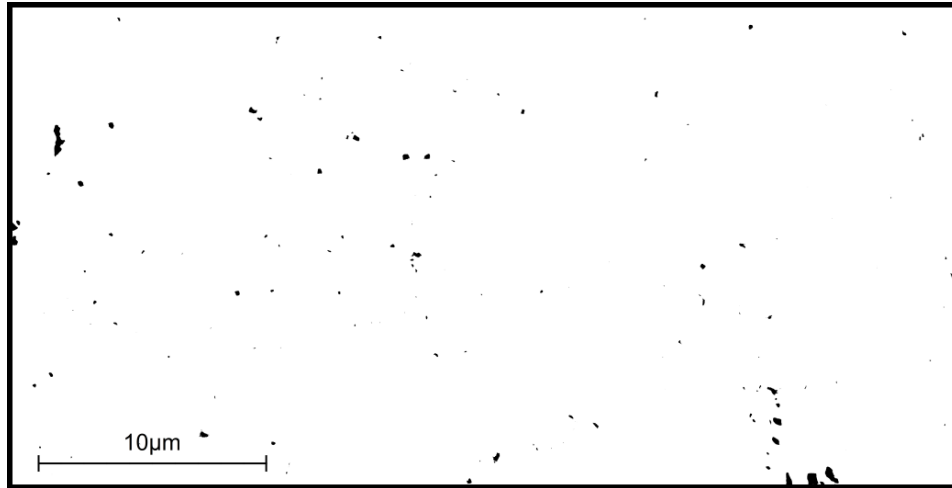


**Figure 49.** SEM image of heat treated HPT-Pd segmented into black and white

SEM yields by far the largest values for vacancy concentrations compared to those derived from density measurements and DSC. This might be due to (i) remnants of the polishing agent ( $\text{Al}_2\text{O}_3$ ) at the sample surface (see Fig. 50) and the inability to distinguish them from pores in the SEM image and (ii) scratches in the sample surface. The large particle of  $\text{Al}_2\text{O}_3$  shown in Fig. 50 is broken into smaller pieces which scatter around the parent particle. Due to the preceding heat treatment the samples are of very low hardness and the creation of scratches upon polishing cannot be stopped. Few “pores” in Fig. 49 (see ragged shapes in upper left and lower right corner) might originate therefrom rather from vacancies. Therefore the SEM method is prone to overestimate the actual vacancy concentration.

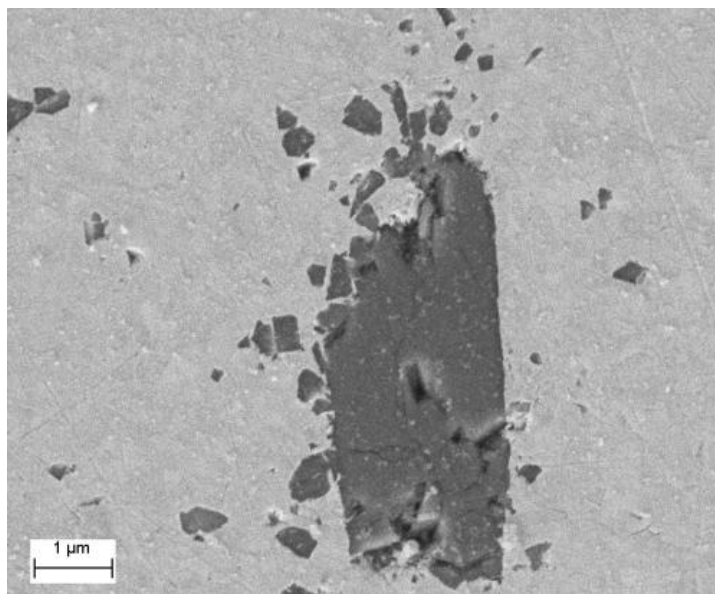


**Figure 50.** Remnants from the polishing agent at the sample surface, like the  $\text{Al}_2\text{O}_3$  particles seen here, contribute to the overestimation of vacancy concentrations derived by segmentation.

### 3.8 Density measurements

Density measurements were performed on samples Pd K, L, Q and R by weighing in four different media,  $\text{N}_2$ , air, Ar and  $\text{C}_2\text{H}_5\text{OH}$  (ethanol) using a Sartorius SE2 ultramicroscales (display accuracy  $0.1 \mu\text{m}$ ).

Measurements under air and Ar were conducted in ambient atmosphere and in a glove box, respectively. For measurements in ethanol a glass was filled and placed on a pedestal directly above the weighing pan. A holder was formed out of Al wire and fixed onto the weighing pan. Onto the holder a cage was hung to reach down into the ethanol.

To remove dirt and an oxidized surface layer the samples were chemically cleaned in a mixture of  $\text{H}_2\text{SO}_4:\text{HNO}_3:\text{H}_2\text{O}$  (volume ratio 2:2:1) before the measurements followed by rinsing with water and cleaning with ethanol in an ultrasonic bath.

The density of air was calculated as the average from two different formulas [73, 74] incorporating temperature, pressure and relative humidity. For measurements in  $\text{N}_2$  and Ar atmosphere gas density was calculated from the ideal gas law by recording pressure  $p$  and

**Table 9.** Average values of densities for the four media used

	N <sub>2</sub>	air	Ar	C <sub>2</sub> H <sub>5</sub> OH
$\rho_{av}$ kg m <sup>-3</sup>	1.1085	1.1721	1.6165	786.91 (23 °C)

temperature  $T$  at each measuring point.

$$\rho = \frac{p}{R_S T} \quad (32)$$

$R_S$  denotes the specific gas constant defined as

$$R_S = \frac{R}{M_L} \quad (33)$$

where  $R$  is the ideal gas constant and  $M_L$  the molar mass of the corresponding gas.

Table 9 gives average values for the densities. For all measurements in ethanol the density of 786.91 kg m<sup>-3</sup> at 23 °C was used. For all media a buoyancy correction was applied to the scales' reference weight to consider changes in the reference weight's apparent mass  $M_a$  compared to its apparent mass  $M_a^{ref}$  in air of standard density (1.2 kg m<sup>-3</sup>) used for basic calibration. The corrected apparent sample mass was calculated as

$$m_a^{corr} = m_a \cdot \frac{M_a}{M_a^{ref}}. \quad (34)$$

Figure 51 shows a graph of the results for sample Pd R including a straight line fit, from which the sample density was extracted as described in section 2.10. Using this density as reference for calculating the vacancy concentration for the three other samples the results show the following trend, see Table 10. Pd R exhibits the highest (11989.9 kg m<sup>-3</sup>) and Pd L the lowest (11884.4 kg m<sup>-3</sup>) density of all samples; densities of Pd K (11919.5 kg m<sup>-3</sup>) and Pd Q (11902.3 kg m<sup>-3</sup>) lie between the former values. By comparing the values with the different

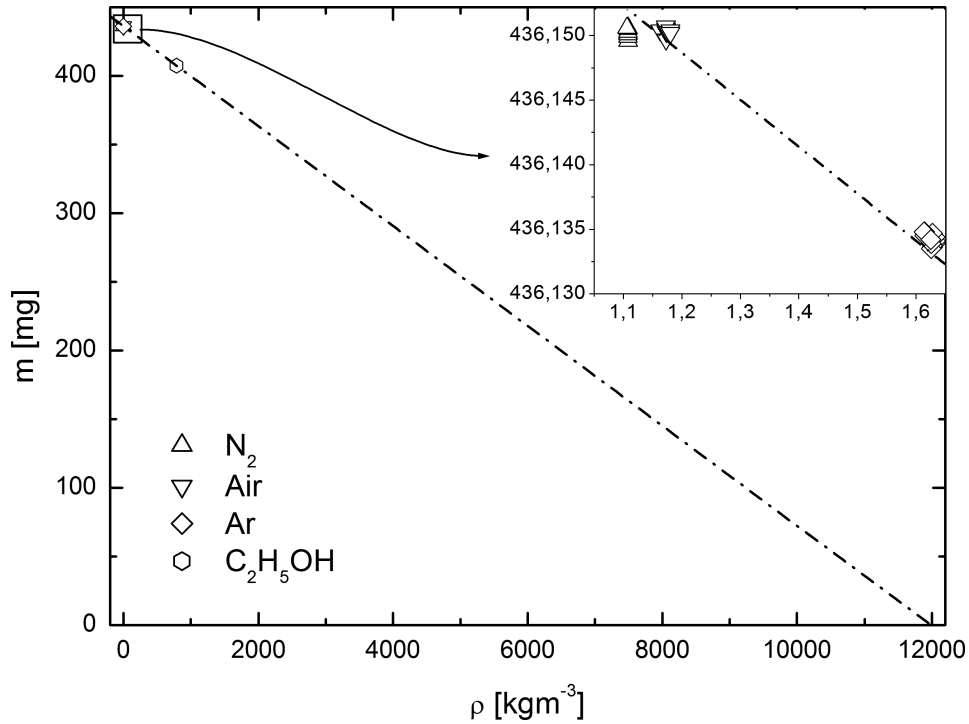


**Figure 51.** Apparent mass of Pd R in four media of different density. The intersection of the best-fit straight line with the horizontal axis is equal to the sample density.

procedures of sample treatment the following pattern arises: Pd R (not H-loaded, not HPT-deformed) gives a reference value for the density and vacancy concentration in pure Pd. Both deformation by HPT (Pd K) alone and H-loading (Pd Q) alone produce vacancy concentrations of 0.59 at% and 0.73 at%, respectively, compared to Pd R. H-loading and HPT-deformation afterwards (Pd L) brings about the highest vacancy concentration of 0.88 at%. The formation of a large number of vacancies by SPD and especially during HPT is well known [75]. High concentrations of 0.1–1 at% for vacancies formed by hydrogenation exceeding the concentration of thermal vacancies in Pd were reported by Sakaki et al. [76]. The low value of 0.73 at% reported in this work may be explained by the heat treatment (1 h at 1073 K) before SEM investigations preceding density measurements, which allowed a part of the vacancies to migrate to the sample free surface thereby increasing sample density.

It is considered that substantial improvement of the density measurements can be achieved by including weighings in high density fluids, e. g. gaseous sulfurhexafluoride (SF<sub>6</sub>,  $\rho$  =

**Table 10.** Densities of differently treated Pd samples together with subsequent vacancy concentrations according to Table 6 on p. 45. The  $d$ 's denote the uncertainties which were calculated by Gauß' law for the propagation of errors.

		K (HPT)	L (loading + HPT)	Q (loading)	R (reference)
$\rho$	$\text{kg m}^{-3}$	11919.5	11884.4	11902.3	11989.9
$d_\rho$	$\text{kg m}^{-3}$	0.9	0.9	0.8	0.6
$c_v$	at%	0.59	0.88	0.73	-
$d_{c_v}$	at%	0.01	0.01	0.01	-

$6.14 \text{ kg m}^{-3}$ ) or metals being liquid at RT. Although the accuracy is good (uncertainty of density  $d_\rho$  and of vacancy concentration  $d_{c_v}$  on the sixth and second digit, respectively, see Table 10) a glimpse at Fig. 51 clearly demonstrates that measurements in high density media are highly desirable. First tests were done in mercury (Hg), though proved impractical due to the solubility of Pd in Hg. In selecting the fluid the following criteria need to be taken into account: (i) the material to be weighed must be insoluble in the fluid and the fluid must not react in any way with the sample, (ii) the fluid must not wet the cage in order to eliminate compromising capillary forces acting on the cage where it penetrates the fluid-air interface.

## 4 Summary and outlook

### 4.1 Summary

Samples of Pd were loaded with H up to a concentration of  $x = [\text{H}]/[\text{Pd}] = 0.78$ . Weighing of  $\text{PdH}_{0.78}$  stored at RT under air showed a complete desorption of interstitial H within four days in case of a low-mass sample with initial thickness of 0.8 mm. In case of an identically prepared sample of more than double thickness (1.7 mm) desorption of H proceeded more slowly and was surprisingly not finished after 28 days. Furthermore the speed of desorption decreased in a non-monotonic way, which might hint at different predominant desorption processes or faster desorption in the two-phase  $\alpha + \beta$  region compared to the single-phase  $\beta$ -region.

Microhardness measurements on  $\text{PdH}_{0.78}$  yielded a drop in Vickers hardness from 1.2 GPa to 1 GPa, i. e. 17 % within the first four days of exposure to RT. The former value was assigned to the  $\beta$ -phase, the latter to a mixture of  $\alpha$  and  $\beta$ -phase at the right boundary of the miscibility gap.

First hydrogenation experiments on Ti proved the Sieverts apparatus employed [61] to be well suited for this task. Qualitative DSC measurements on  $\text{TiH}_{1.91}$  agree very well with results found in literature. Further it was shown that HPT is a powerful method for high-grade plastic deformation of highly brittle materials like  $\text{TiH}_2$  without causing material failure.

In order to investigate the influence of deformation temperature on the formation of Vac-H clusters in PdH during plastic deformation, samples of  $\text{PdH}_{0.78}$  were processed by HPT at temperatures of liquid  $\text{N}_2$  and frozen  $\text{CO}_2$ , i. e. 77 K and 195 K, respectively. In the DSC measurements of samples deformed at 77 K, the exothermic peak at 482 K ascribed to the disintegration of Vac-H clusters [61] was not present. This was attributed either to a lack of mobility of interstitial H atoms at 77 K or to the presence of a H-ordered low-temperature phase related to the 50 K anomaly in PdH. In samples deformed at 195 K the peak at 482 K was registered, though it markedly broadened and considerably lost intensity after annealing at RT

for more than half a year. These results suggest that Vac-H clusters in Pd are not stable at RT but in fact disintegrate with time.

Investigations by SEM showed the existence of a large number of pores at the free surface of HPT-deformed  $\text{PdH}_{0.73}$  subjected to extra heat treatment. From the images a high local vacancy concentration of  $2.8 \cdot 10^{-2}$  was derived for HPT-deformed  $\text{PdH}_{0.73}$  and  $3.1 \cdot 10^{-3}$  for pure HPT-deformed Pd.

These results are corroborated by density measurements, which yielded the highest vacancy concentration for H-loaded and deformed Pd ( $c_v = 0.88 \cdot 10^{-2}$ ) and followed by H-loaded non-deformed Pd ( $c_v = 0.73 \cdot 10^{-2}$ ) and non-loaded deformed Pd ( $c_v = 0.59 \cdot 10^{-2}$ ). Surprisingly sole hydrogenation resulted in a higher vacancy concentration than deformation by HPT to extremely high grades of 30 rot.

## 4.2 Outlook

It would appear that additional data is necessary before the formation mechanisms of Vac-H clusters in Pd during HPT at different temperatures can be fully understood. Further HPT experiments at various higher deformation temperatures between 195–323 K and subsequent DSC measurements are under way.

Further substantiating of the attribution of the exothermic DSC peak at 482 K to the disintegration of Vac-H clusters [16] could be achieved by a precise determination of H concentration in the course of heating. Additionally, it is still unclear how much H trapped at lattice defects remains in the host lattice after desorption of interstitial H. In principle, this can be done indirectly by measuring the total amount of H after loading and subtracting the amount of H trapped at interstitial sites, which can be precisely derived from lattice parameter measurements. However, loss of H during HPT or X-ray measurements compromise exact results. To circumvent these problems, the method Prompt Gamma Activation Analysis (PGAA) is planned to be used for a *direct* determination of the total amount of H trapped at lattice defects. PGAA

is non-destructive so further use of samples is possible. A first experiment at the Budapest Neutron Center is scheduled.

Additionally a Small Angle Neutron Scattering (SANS) experiment could provide information on the number and size distribution of pores located in the sample interior not detectable by SEM.

To further assess the concentration of vacancies introduced by different combinations of sample treatment Positron Annihilation Spectroscopy (PAS) might provide valuable information. This method allows to determine (i) the total concentration of vacancies, (ii) the type of vacancy agglomerates, i. e. the number of vacancies per agglomerate, and (iii) in combination with Doppler coincidence spectroscopy to retrieve information about the nature and number of atoms surrounding the vacancies.

Substantial improvement in accuracy of vacancy concentrations derived from density measurements is considered to be achieved by including weighings in high density fluids like gases or metals being liquid at RT. First tests were done in Hg, though proved impractical due to solubility of Pd in Hg.

## 5 Appendices

### 5.1 Appendix I

The read out from the Sartorius M3P microbalance was controlled by the following shell script.

```
#!/bin/bash
cp /dev/ttyS0 mass.dat &

count=0

while [ $count -le N ]
do
date +%c%t%s >> time.dat
cp print.bin /dev/ttyS0
sleep ts
count=$((count+1))
done

exit 0
```

The mass values are written to the file `mass.dat` and corresponding times to `time.dat`. The readout frequency is controlled via `sleep ts` where `t` denotes the period length in seconds. The balance command to read out the value is sent in the file `print.bin`, which contains the four byte sequence `Esc P cr nl`, where `P` is the actual print command, confer the manual [77]. The total number of readouts is given by `N`. Invoking the script is done via the command `./filename`.

## 5.2 Appendix II

**Palladium rod, 6.35mm (0.25in) dia, 99.95% (metals basis)**

**Stock Number: 12557**

**Lot Number: A14U007**

### **Typical Analysis of Starting Material**

Pd		99.99+ % (by difference)			
Pt	22	Rh	ND	Ru	ND
Ir	ND	Au	13	Ag	ND
Os	ND	Ca	19	Fe	8
Cu	3	Ni	ND	Zn	1
Mo	ND	Cd	ND	W	ND
Pb	ND	Cr	2	Mn	ND
Al	2	Mg	ND	Sn	ND
As	ND	Sb	ND	Bi	ND
Te	ND	B	ND	Co	ND
Si	ND	P	ND	Na	ND
Se	ND				

Values given in ppm unless otherwise noted

ND: Not detected

**Figure 52.** Certificate of analysis of Pd 99.95at% (AlfaAesar)

**Titanium rod, 6.4mm (0.25in) dia, 99.99% (metals basis)**

**Stock Number: 14001**

**Lot Number: E25R015**

**Analysis**

Ag	< 0.05	Al	0.5	As	0.06	Au	< 0.05
B	< 0.01	Ba	< 0.005	Be	< 0.005	Bi	< 0.01
Br	< 0.05	C	11	Ca	< 0.2	Cd	< 0.05
Ce	< 0.005	Cl	0.06	Co	0.009	Cr	0.375
Cs	< 0.01	Cu	0.445	F	< 0.05	Fe	3
Ga	< 0.05	Ge	< 0.05	H	1	Hf	< 0.01
Hg	< 0.1	I	< 0.01	In	< 0.05	Ir	< 0.01
K	< 0.01	La	< 0.005	Li	< 0.005	Mg	< 0.05
Mn	0.0175	Mo	< 0.05	N	< 10	Na	< 0.01
Nb	< 0.2	Nd	< 0.005	Ni	0.6	O	169
Os	< 0.01	P	0.0265	Pb	< 0.01	Pd	< 0.01
Pt	< 0.05	Rb*	< 5	Re	< 0.01	Rh	< 0.15
Ru	< 0.01	S	5	Sb	0.11	Sc	< 0.05
Se	< 0.05	Si	0.4	Sn	0.06	Sr*	< 3000
Ta**	< 5	Te	< 0.05	Th	< 0.0005	Tl	< 0.01
U	< 0.0005	V	0.25	W	< 0.01	Y*	< 200
Zn	< 0.05	Zr	0.7	Yb	< 0.005	Zn	< 0.05
Zr	0.7						

Values are given in ppm unless otherwise noted

Carbon , Hydrogen, Nitrogen, Oxygen, and Sulfur determined LECO

All other elements determined by GDMS

\* Ion interference

\*\* Instrument contamination

**Figure 53.** Certificate of analysis of Ti 99.99at% (AlfaAesar)

## References

- [1] Zehetbauer, M.J., and Zhu, Y.T., (ed.) Bulk Nanostructured Materials, Wiley-VCH, Weinheim, Germany (2009).
- [2] Valiev, R., Islamgaliev, R., and Alexandrov, I. *Prog. Mater. Sci.* **45**, 103–189 (2000).
- [3] Valiev, R. and Langdon, T. *Prog. Mater. Sci.* **51**, 881–981 (2006).
- [4] Blewitt, T., Coltman, R., Klabunde, C., and Noggle, T. *J. Appl. Phys.* **28(6)**, 639–644 (1957).
- [5] Sosin, A. and Rachal, L. *Phys. Rev.* **130(6)**, 2238–2248 (1963).
- [6] Darling, K., Chan, R., Wong, P., Semones, J., Scattergood, R., and Koch, C. *Scr. Mater.* **59(5)**, 530 – 533 (2008).
- [7] Setman, D., Lattice defects in HPT processed fcc nanometals studied by differential scanning calorimetry, PhD thesis, University of Vienna, Faculty of Physics (2010).
- [8] Fukai, Y. and Okuma, N. *Jpn. J. Appl. Phys.* **32**, 1256–1259 (1993).
- [9] Fukai, Y. and Okuma, N. *Phys. Rev. Lett.* **73(12)**, 1640–1643 (1994).
- [10] Fukai, Y., Mizutani, M., Yokota, S., Kanazawa, M., Miura, Y., and Watanabe, T. *J. Alloys Compd.* **356–357**, 270–273 (2003).
- [11] Tavares, S., Miraglia, S., Fruchart, D., dos Santos, D., Ortega, L., and Lacoste, A. *J. Alloys Compd.* **372(1-2)**, L6–L8 (2004).
- [12] Fukai, Y. *J. Alloys Compd.* **356–357**, 263–269 (2003).
- [13] Fukai, Y. *Phys. Scr.* **T103**, 11–14 (2003).
- [14] Kirchheim, R. *Acta Mater.* **55(15)**, 5129–5138 (2007).
- [15] Zehetbauer, M. *Key. Eng. Mater.* **97–98**, 287–306 (1994).
- [16] Krystian, M., Setman, D., Mingler, B., Krexner, G., and Zehetbauer, M. *Scr. Mater.* **62**, 49–52 (2010).
- [17] Kirchheim, R. *Solid State Phys.* **59**, 203–291 (2004).
- [18] Kirchheim, R. *Acta Mater.* **55(15)**, 5139–5148 (2007).
- [19] Fukai, Y. (2005) The Metal-Hydrogen System, Springer-Berlin, 2<sup>nd</sup> edition.
- [20] Alefeld, G., and Völkl, J., (ed.) Hydrogen in Metals I - Basic Properties, Springer-Berlin (1978).

- [21] Alefeld, G., and Völkl, J., (ed.) Hydrogen in Metals II - Application-Oriented Properties, Springer-Berlin (1978).
- [22] Flanagan, T. and Oates, W. *Annu. Rev. Mater. Sci.* **21**, 269–304 (1991).
- [23] Mine, Y., Tsumagari, T., and Horita, Z. *Scr. Mater.* **63(5)**, 552–555 (2010).
- [24] Cizek, J., Prochazka, I., Danis, S., Cieslar, M., Brauer, G., Anwand, W., Kirchheim, R., and Pundt, A. *J. Alloys Compd.* **446–447**, 479–483 (2007).
- [25] Saito, Y., Utsunomiya, H., Tsuji, N., and Sakai, T. *Acta Mater.* **47(2)**, 579–583 (1999).
- [26] Valiev, R., Krasilnikov, N., and Tsenev, N. *Mater. Sci. Eng. A* **137(C)**, 35–40 (1991).
- [27] San-Martin, A. and Manchester, F. *Bull. Alloy Phase Diagr.* **8(1)**, 30 (1987).
- [28] Gottstein, G. (1998) *Physikalische Grundlagen der Materialkunde*, Springer-Berlin.
- [29] Verhoeven, J. (1975) *Fundamentals of Physical Metallurgy*, John Wiley & Sons.
- [30] Hall, D. and Bacon, D. (2001) *Introduction to Dislocations*, Butterworth-Heinemann, 4<sup>th</sup> edition.
- [31] Heumann, T. (1992) *Diffusion in Metallen*, Springer-Berlin.
- [32] Stüwe, H. *Z. Metallkd.* **56**, 633–642 (1965).
- [33] Zehetbauer, M. and Seumer, V. *Acta Metall. Mat.* **41**, 577–588 (1993).
- [34] Zehetbauer, M. *Acta Metall. Mat.* **41**, 589–599 (1993).
- [35] Schafner, E., Investigation of microstructural evolution in large strain worked metals by X-ray Bragg profile analysis, PhD thesis, University of Vienna, Faculty of Physics (1998).
- [36] Valiev, R., Estrin, Y., Horita, Z., Langdon, T., Zehetbauer, M., and Zhu, Y. *JOM - J. Min. Met. Mater. S.* **58**, 33–39 (2006).
- [37] Valiev, R., Korznikov, A., and Mulyukov, R. *Mater. Sci. Eng. A* **168**, 141–148 (1993).
- [38] Skripnyuk, V., Rabkin, E., Estrin, Y., and Lapovok, R. *Int. J. Hydrogen Energy* **34**, 6320–6324 (2009).
- [39] Estrin, Y. *Mater. Sci. Forum* **503–504**, 91–98 (2006).
- [40] Zehetbauer, M., Stüwe, H., Vorhauer, A., Schafner, E., and Kohout, J. *Adv. Eng. Mater.* **5(5)**, 330–337 (2003).
- [41] Hall, E. *Proc. Phys. Soc.* **B64(9)**, 742–747 (1951).
- [42] Petch, N. *J Iron Steel Inst* **174**, 25–28 (1953).

- [43] Valiev, R., Alexandrov, I., Zhu, Y., and Lowe, T. *J. Mater. Res.* **17**(1), 5–8 (2002).
- [44] Zhilyaev, A., Nurislamova, G., Kim, B.-K., Baró, M., Szpunar, J., and Langdon, T. *Acta Mater.* **51**, 753–765 (2003).
- [45] Stüwe, H. (2004) In M. Zehetbauer and V. Z. Ruslan, (ed.), *Nanomaterials by Severe Plastic Deformation - NanoSPD2*, Wiley-VCH pp. 55–64.
- [46] Graham, T. *P. R. Soc. London* **16**, 422–427 (1867).
- [47] McLennan, K., *Structural Studies of the Palladium-Hydrogen System*, PhD thesis, Griffith University, School of Science, 2005.
- [48] Dornheim, M., Klassen, T., and Bormann, R. *Jap. Soc. Promotion Sci.* p. L18 (2004).
- [49] Sieverts, A. *Z. Metallkd.* **21**(2), 37–46 (1929).
- [50] Chandra, D., Reilly, J., and Chellappa, R. *JOM - J. Min. Met. Mater. S.* **58**, 26–32 (2006).
- [51] Pundt, A. (2005) *Nanoskalige Metall-Wasserstoff-Systeme*, Universitätsverlag Göttingen.
- [52] Tal-Gutelmacher, E., Gemma, R., Pundt, A., and Kirchheim, R. *Acta Mater.* **58**(8), 3042 – 3049 (2010).
- [53] Numakura, H. and Koiwa, M. *Acta. Metall. Mater.* **32**(10), 1799 – 1807 (1984).
- [54] Kappesser, B. and Wipf, H. *J. Phys. IV.* **6**, C8–73 (1996).
- [55] Simmons, R. and Balluffi, R. *Phys. Rev.* **117**(1), 52–61 (1960).
- [56] Watanabe, K., Okuma, N., Fukai, Y., Sakamoto, Y., and Hayashi, Y. *Scr. Mater.* **34**(4), 551 – 557 (1996).
- [57] Osono, H., Kino, T., Kurokawa, Y., and Fukai, Y. *J. Alloys Compd.* **231**(1-2), 41–45 (1995).
- [58] Vekilova, O. Y., Bazhanov, D. I., Simak, S. I., and Abrikosov, I. A. *Phys. Rev. B* **80**(2), 024101 (2009).
- [59] Würschum, R., Kübler, A., Gruss, S., Acharwaechter, P., Frank, W., Valiev, R., Mulyukov, R., and Schaeffer, H.-E. *Ann. Chim. Fr.* **21**, 471–482 (1996).
- [60] Lu, G. and Kaxiras, E. *Phys. Rev. Lett.* **94**, 155501 (2005).
- [61] Krystian, M. *Meas. Sci. Technol.* (2011) in press.
- [62] Kropik, H., *Wasserstoffspeicherung in SPD-nanokristallisierten ZK60 Magnesium-legierungen*, Master's thesis, University of Vienna, Faculty of Physics (2008).
- [63] Wassermann, G. (1965) *Praktikum der Metallkunde und Werkstoffprüfung*, SpringerBerlin.

- [64] Goodhew, P., Humphreys, J., and Beanland, R. (2001) Electron microscopy and analysis, Taylor & Francis, 3<sup>rd</sup> edition.
- [65] Höhne, G., Hemminger, W., and Flammersheim, H.-J. (1996) Differential Scanning Calorimetry - An Introduction for Practitioners, Springer-Berlin.
- [66] Kissinger, H. *Annal. Chem.* **29**, 1702–1706 (1957).
- [67] Vorhauer, A. and Pippan, R. *Scr. Mater.* **51(9)**, 921 – 925 (2004).
- [68] Blaschko, O. *J. Less-Common Met.* **100**, 307–320 (1984).
- [69] Wu, E., Kennedy, S., Gray, E. A., and Kisi, E. *J. Phys.: Condens. Matter* **8(16)**, 2807–2813 (1996).
- [70] Illeková, E., Harnúšková, J., Florek, R., Simančík, F., Matko, I., and Švec Sr., P. *J. Therm. Anal. Calorim.* (2010) in press.
- [71] dos Santos, D., Miraglia, S., and Fruchart, D. *J. Alloys Compd.* **291**, L1–L5 (1999).
- [72] Stoyan, D. and Mecke, J. (1983) Stochastische Geometrie: Eine Einführung, Akademie Verlag Berlin.
- [73] Picard, A., Davis, R., Gläser, M., and Fujii, K. *Metrologia* **45**, 149–155 (2008).
- [74] Jones, F. *J. Res. Natl. Inst. Stan.* **83**, 419 (1978).
- [75] Zehetbauer, M., Steiner, G., Schafler, E., Kroznikov, A., and Korznikova, E. *Mater. Sci. Forum* **503–504**, 57–64 (2006).
- [76] Sakaki, K., Yamada, T., Mizuno, M., Araki, H., and Shirai, Y. *Mater. Trans.* **43(11)**, 2652–2655 (2002).
- [77] Manual Sartorius Microbalance M3P Date retrieved: January 3, 2011, [www.sartorius-mechatronics.com/uploads/tx\\_sartoriusmechpdf/MAN-M3P\\_M3P-000V001-d.pdf](http://www.sartorius-mechatronics.com/uploads/tx_sartoriusmechpdf/MAN-M3P_M3P-000V001-d.pdf).

## Acknowledgements

Finally, I would like to mention and, at the same time, thank a few people, who supervised me during writing this work and performing the measurements.

First of all are to name Maciej Krystian, Michael Zehetbauer and Gerhard Krexner. Maciej Krystian intensively looked after me especially during the beginning of the work and was (is) always open for questions. Michael Zehetbauer allowed me to enter the field of metal-hydrogen systems. He supported me financially and offered me the opportunity to publish a part of the results. Gerhard Krexner answered many of my questions during long discussions, supported me financially on the MH2010 and took the position of the official supervisor.

The sample preparation and the measurements were usually not work of one solitary person:

Daria Setman helped me with the DSC measurements and was always available in case of difficulties. Susi Kahofer's support with HPT deformations in Leoben was very helpful. Together with Christian Rentenberger I spent several hours at the SEM searching for pores. Martina Rohrer had polished the samples beforehand. The communication with the microscopes would not have been possible without Walter Penits. Also it was him who came up with the idea for the logarithmic plot of the desorption graphs.

I would like to express thanks to all members of the group Nanostructured Materials for quite a few helpful hints and for the great support in binding the hard copies!

# Matthias Bönisch

## *Curriculum Vitae*

### Education

- 2005–2011     *Studies in Physics*, University of Vienna, Austria  
Diploma thesis: *On the influence of hydrogen on the stability of lattice defects in metals*  
supervisors: Prof. Dr. M. Zehetbauer, Prof. Dr. G. Krexner  
  
studies abroad at University of Kuopio, Finland, autumn 2008
- 2010/07     *Summer School on Materials for the Hydrogen Society 2010*  
ISSP, Chernogolovka (Russia)
- 2010/06     *CETS 2010 - Central European Training School on Neutron Scattering*  
BNC, Budapest (Hungary)
- 2004     *School leaving exam*, with distinction, 2004  
humanistic branch at “GRG XVI”, Vienna, Austria

### Conference contributions

- 2010/07     Talk: *Stabilization of Lattice Defects in HPT-deformed Pd*  
M. Bönisch, M. Krystian, D. Setman, G. Krexner, M. Zehetbauer  
MH2010, Moscow (Russia)
- 2010/07     Poster: *Stabilization of Lattice Defects in HPT-deformed Pd*  
M. Bönisch, M. Krystian, D. Setman, G. Krexner, M. Zehetbauer  
ISMANAM 2010, Zürich (Switzerland)

### Extracurricular

- 2004–2005     Civilian Service: Support of physically and mentally disabled youths, Vienna
- 2009     Social tutoring of first year students

<i>Citizenship:</i>	Austria
<i>Date and place of birth:</i>	13.08.1986, Vienna